

"OPTICAL BIOSENSING PLATFORM ASSISTED BY ARTIFICIAL INTELLIGENCE, DEEP LEARNING."



(Versión definitiva. Incluye cambios sugeridos por revisores) Firma del Director:

Dr. Eden Morales Narváez

Fernando Avie Vega Firma del Co Director:

Dr. Fernando Arce Vega

Tesis que para obtener el grado de Doctorado en Ciencias (Óptica)

Presenta: Diana Lorena Mancera Zapata León · Guanajuato · México Mayo 27 de 2025

Acknowledgments

I would like to express my deepest gratitude to my advisor, Eden, for his unwavering support and trust in me over these six years. His guidance and teaching have been crucial in my professional and personal development.

I am also grateful to Professor Fernando Arce for his patience and support.

To Ulises and my other friends at CIO and in León, Guanajuato, thank you for your steadfast support and for being my family away from home. Your companionship has been a constant source of strength and joy, helping me to reach this point.

To Ch, Vinagre, and K, my lifelong best friends, your support, even from afar, has meant more to me than words can express. You always believed I would finish this thesis, and that belief has been a tremendous source of encouragement.

To Caro, Eve, Triglis, and my other new friends in Guadalajara, thank you for easing this transition in my life, for welcoming me with open arms, and for making me feel like one of your own. Your warmth, kindness, and daily reminders to complete my thesis have made this new chapter in my life truly special.

Last but not least, to my mother and brother, thank you for your example of tenacity and courage, for your unwavering support, and for helping me become the woman I am today.

I am also deeply grateful to CONACYT for the financial support that made it possible for me to pursue this PhD, to the DGAPA-UNAM project (Grant No. PAPIIT-IT100124) and Fundación Marcos Moshinsky UNAM for their invaluable assistance.

Abstract

Biosensors are analytical devices designed to detect specific target molecules with high selectivity and sensitivity. The selectivity of a biosensor is crucial, as it determines the system's ability to identify a specific analyte among numerous other substances in a sample. Low selectivity in biosensors can lead to false positives, reducing their reliability and effectiveness in biomedical applications. This issue arises because biological samples often contain various biomolecules that may cause an interference in the sensing surface and avoid the detection of the target analyte.

Recent research has demonstrated that computational methods, such as machine learning algorithms hold significant potential for enhancing the analytical performance of biosensing platforms. By detecting complex patterns within noisy signals, computation can provide insights across various domains, including medical data, environmental monitoring, and traffic signal analysis. This doctoral research aimed to enhance biosensing systems using artificial intelligence, specifically Deep Learning, by implementing neural models that improved their analytical performance. We studied a nanophotonic immunoassay for diagnosing bacterial vaginosis, achieving clinical sensitivity and specificity of approximately 96.29% (n = 162). In this context, this thesis demonstrates that an AI-assisted real-time biosensing platform eliminates the need for biomarker concentration as well as threshold determination, and also enhances clinical sensitivity and specificity, reaching up to 100%.

Objectives

General Objective

 Implement a deep learning model to assist and optimize the analytical performance of a biosensing system, in particular for bacterial vaginosis diagnosis (using sialidase as a biomarker).

Specific Objectives

- Develop and implement a deep neural network model using the "K-fold cross-validation" method, trained with experimental data. Initially, this will involve data from sialidase (SLD) detection. Several neural network models will be assessed.
- Train the developed deep neural network models with experimentally obtained data to recognize and/or estimate SLD levels related to positive or negative samples.
- Validate the performance of the neural network using test data to enhance the specificity and sensitivity of the biosensing system.

Table of Contents

	Acknowledgments	2
	et	
Objecti	ives	5
Spec	rific Objectives	5
Gene	eral Objective¡Error! Marcado	r no definido.
SCIEN	TIFIC PRODUCTION	11
PUB	LICATIONS	11
PRO	CEEDINGS	12
COV	VER ART PUBLISHED	12
VOL	LUNTEERING	13
Chapte	r 1	14
Theore	tical framework	14
1.1.	Definition of a biosensor	14
1.2.	Physical phenomena involved in optical biosensor	15
Ph	notoluminescence	15
Fö	orster resonance energy transfer (FRET)	16
1.3.	GO and operating mechanism of FRET-GO based biosensor	19
1.4.	Bacterial Vaginosis	21
1.5.	Artificial intelligence (AI)	23
M	achine learning.	23
De	eep Learning	23
1.6.	Artificial Neural Networks (ANNs) types	26
Fe	eed forward Neural Network (FNN)	27
Co	onvolutional Neural Network (CNN)	27
Re	ecurrent Neural Networks (RNNs)	28
Lo	ong Short-Term Memory (LSTM)	28
Ga	ated Recurrent Units (GRUs) Error! Marcado	r no definido.
Ge	enerative Adversarial Networks (GANs): Error! Marcado	r no definido.
M	ultilayer Perceptrons (MLPs)	28
1.7.	K-fold cross validation	29
1.8.	Principal Component Analysis (PCA)	29
1.9.	Evaluation metrics	30
Co	onfusion Matrix	30

F ₁ score	32
REFERENCES	33
Chapter 2	35
Artificial intelligence in biosensing field: State of the art	35
REFERENCES	38
Chapter 3	40
Experimental set up	40
3.1. Neural Network Implementation for Sialidase detection.	40
3.1.1. Reagents and equipment	40
3.1.2. Dataset collection	40
3.2.1. Normalization	42
3.4.1. ANNS implementation	43
3.5. Feature selection.	44
3.6. Determination of clinical sensitivity and specificity.	44
REFERENCES	45
Chapter 4.	46
Results and discussion	46
Chapter 5	56
Conclusions	56
Chapter 6	57
Appendix	57
6.1. Performance of the 1D-CNN architecture fed with groups of 20 and 30 min	
intervals.	
6.2. Image Segmentation Process Using U-NET Architecture	
6.3. Kinetic Binding Constants	
Association Constant (Ka)	59
Dissociation Constant (Kd)	60

List of Figures

Figure 1. Schematic representation of different blocks integrating a biosensor15
Figure 2. Typical Jablonski diagram to illustrate photoluminescent processes16
Figure 3. FRET A
Figure 4. Allotropes of Carbon
Figure 5. Representation of the structure of GO
Figure 6. Operational mechanism of the biosensing platform21
Figure 7. Bacterial Vaginosis illustration.
Figure 8. Visual Breakdown of Key Areas in Artificial Intelligence24
Figure 9. Main Parts of a Neural Network
Figure 10. Schematic diagram of the basic functioning of an artificial neural
network (perceptron)
Figure 11. Neural Networks types.
Figure 12. K-fold Cross Validation
Figure 13. Dimensionality Reduction
Figure 14. Confusion Matrix for binary classification
Figure 15. Sample Preparation and Biosensing Platform for SLD Detection41
Figure 16. A. Dataset matrix B. Dataset splitting
Figure 17. PCA and distances between the classes BV+ and BV- (for the complete
data and for different times data sets)
Figure 18. Bar chart depicting the performance of the 1D-CNN architecture fed
with different combinations of data groups
Figure 19. The resultant confusion matrix of the training, 70% of the data was used
for the training set, 15% for the validation set, and 15% for the testing set52
Figure 20. Confusion matrices for each fold in MLP architecture53
Figure 21. Confusion matrices for each fold in CNN architecture54
Figure 22. Confusion matrices for each fold in LSTM architecture54
Figure 23. Confusion matrices for each fold in B-LSTM architecture55
Figure 24. Paper-Based Microfluidic Analytical Device58
Figure 25. Segmentation Process
Figure 26. First predictions of the uPAD shape.

Figure	27. Graphical interface developed for determining association and	
dissocia	ation constants in H-IgG samples, with association and dissociation co	nstants
display	red on the left side	60

List of Tables

Table 1. Machine learning for intelligent biosensing.	36
Table 2. Performances of the tested architectures assessed with 10-fold cross-	
validation	47
Table 3. F ₁ score for each fold in the MLP, LSTM, B-LSTM and 1D-CNN	
architectures	48
Table 4. Performance of the best architecture, the 1D-CNN, for the time groups	G_1 ,
G ₂ , G ₃ and G ₄ .	49
Table 5. Performance of the 1D-CNN architecture fed with different combination	ns
of data groups.	50
Table 6. Results of the training process	52
Table 7. F ₁ Score for each fold in MLP architecture.	53
Table 8. F ₁ Score for each fold in CNN architecture.	54
Table 9. F ₁ Score for each fold in LSTM architecture.	55
Table 10. F ₁ Score for each fold in B- LSTM architecture.	55
Table 11 . Performance of the 1D-CNN architecture fed with groups of 20 min	
intervals.	57
Table 12 . Performance of the 1D-CNN architecture fed with groups of 30 min	
intervals	57

SCIENTIFIC CONTRIBUTIONS

PUBLICATIONS

- Mancera-Zapata, D. L, Rodriguez-Nava, C.; Arce, F. Morales-Narváez, E. Al-Assisted Real-Time Immunoassay Improves Clinical Sensitivity and Specificity. Anal. Chem. 2024, 96, 34, 13756–13761. https://doi.org/10.1021/acs.analchem.4c00764.
- 2. **Mancera- Zapata, D. L**, Saldaña. A.; Celebrating Inclusion and Diversity of Women in Science, ACS Materials Au 2024 4 (2), 107-107, https://pubs.acs.org/doi/10.1021/acsmaterialsau.4c00009.
- 3. Mancera-Zapata, D. L. Avila-Huerta, M. D.; Reach for the Stars Inspiring Latin American Women in STEM. ACS Meas. Sci. Au 2022, 2 (6), 493–494. https://doi.org/10.1021/acsmeasuresciau.2c00060.
- Mancera-Zapata, D. L and Morales-Narváez, E. A Biosensing Platform Based on Graphene Oxide and Photoluminescent Probes: Advantages And Perspectives, Mundo Nano 16(31), 2023. https://doi.org/10.22201/ceiich.24485691e.2023.31.69798
- Ortiz-Riaño. Edwin J. Mancera-Zapata D.L, Ulloa-Ramírez. M. Fernando Arce-Vega, and Morales-Narváez, E. Measurement of Protein Kinetics using a Liquid Phase-Based Biosensing Platform, Analytical Chemistry Article ASAP. 2022. https://doi.org/10.1021/acs.analchem.2c03305.
- 6. Avila-Huerta, M. D.; Ortiz-Riaño, E. J.; **Mancera-Zapata, D.** L.; Cortés-Sarabia, K.; Morales-Narváez, E. Facile Determination of COVID-19 Seroconversion via Nonradiative Energy Transfer. ACS Sens. 2021, 6 (6), 2136–2140. https://doi.org/10.1021/acssensors.1c00795.
- 7. Avila-Huerta, M. D.; Ortiz-Riaño, E. J.; **Mancera-Zapata, D. L.**; Morales-Narváez, E. Real-Time Photoluminescent Biosensing Based on Graphene Oxide-Coated Microplates: A Rapid Pathogen Detection Platform. Anal. Chem. 2020, 92 (17), 11511–11515. https://doi.org/10.1021/acs.analchem.0c02200.
- 8. Ortiz-Riaño, E. J.; Avila-Huerta, M. D.; **Mancera-Zapata, D. L**.; Morales-Narváez, E. Microwell Plates Coated with Graphene Oxide Enable Advantageous Real-Time Immunosensing Platform. Biosens. Bioelectron. 2020, 165, 112319. https://doi.org/10.1016/j.bios.2020.112319.

PROCEEDINGS

- 1. Avila-Huerta MD, Ortiz-Riaño EJ, **Mancera-Zapata DL**, Morales-Narváez E. Real-Time Pathogen Determination by Optical Biosensing Based on Graphene Oxide. Proceedings. 2020;60(1). doi:10.3390/IECB2020-07016
- 2. Ortiz-Riaño EJ, Avila-Huerta MD, **Mancera-Zapata DL**, Morales-Narváez E. Quenching of Fluorescence Caused by Graphene Oxide as an Immunosensing Platform in a Microwell Plate Format. Proceedings. 2020;60(1). doi:10.3390/IECB2020-07017

COVER ART PUBLISHED

- ✓ Analytical Chemistry (September, 2020)
- ✓ ACS Measurement Science Au (December, 2022)
- ✓ Analytical Chemistry (October, 2022)
- ✓ ACS Materials Au 2024 (February ,2024)
- ✓ Analytical Chemistry (August, 2024)



VOLUNTEERING

- Officer of the OPTICA student chapter (President 2022-2023)| Scientific outreach activities at Ilumina Museum (2022-2023)
- \triangleright

Chapter 1.

Theoretical framework

1.1. Definition of a biosensor

Biosensors are analytical devices designed to detect target molecules with high specificity and sensitivity. The basic operation of biosensors involves three main stages, which are represented in Figure 1. The first stage is biological recognition (or biorecognition), which must be performed with high specificity. The next stage is the transduction process, where the biorecognition event is transformed into a quantifiable signal, providing information about changes in a specific physical parameter^{1,2} (in this work, the fluorescence intensity). Finally, this signal is amplified and processed to produce a measurable result like output signal.

It is important to note that biosensors with high sensitivity can generate a signal from minimal fluctuations in the analyte concentration. The smallest amount of analyte that a biosensor can detect is defined as the limit of detection (LOD), which is a key aspect of its analytical sensitivity. In addition, a biosensor with high specificity indicates that the device can recognize and detect only the target analyte among a mixture of different biomolecules, minimizing the possibility of interference from other substances present in the sample. This means that the biosensor is very selective and precise in its biological recognition, ensuring that the results obtained are reliable and accurate for the analyte of interest. Finally, in the third stage, the resultant signal is obtained and interpreted.³

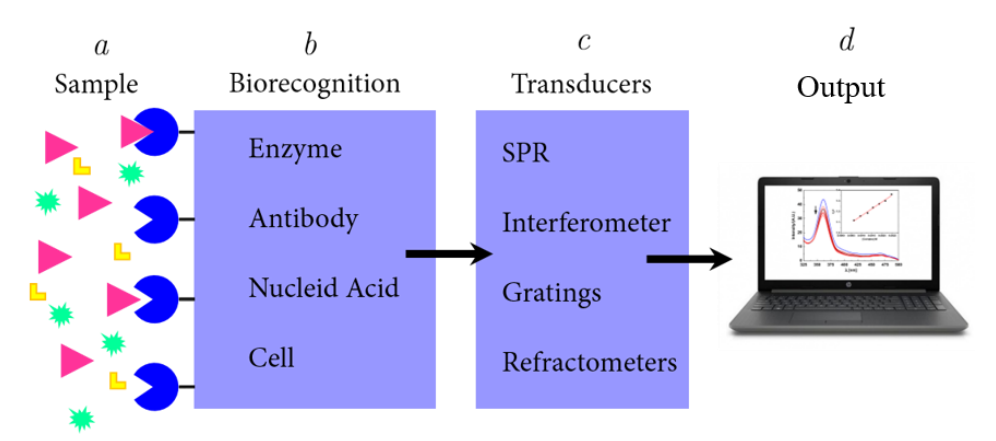


Figure 1. Schematic representation of different blocks integrating a biosensor. a) Sample: substance to be analyzed in which is possible to detect the presence the target analyte. b) Biorecognition: this stage requires elements with high affinity against the target analyte. c) Transducers: A device that converts the measured biological activity into an analytical signal. d) Output: measurable signal indicating the presence of the analyte in the sample. Image taken from ⁵. Unpublished Master's Thesis.

1.2. Physical phenomena involved in optical biosensor

Photoluminescence

Photoluminescence is the emission of light from a material after it has absorbed photons. When the material absorbs light energy, its electrons are excited to a higher energy state. ⁴ The transition of these electrons back to their ground state occurs through the emission of photons. In general, the phenomenon of photoluminescence is classified into two types: fluorescence and phosphorescence, depending on the nature of the excited states. Fluorescence occurs when a transition happens between photoexcited species from their first excited singlet state to their ground state. On the other hand, phosphorescence involves the emission of light from excited triplet states (see Figure 2).⁵

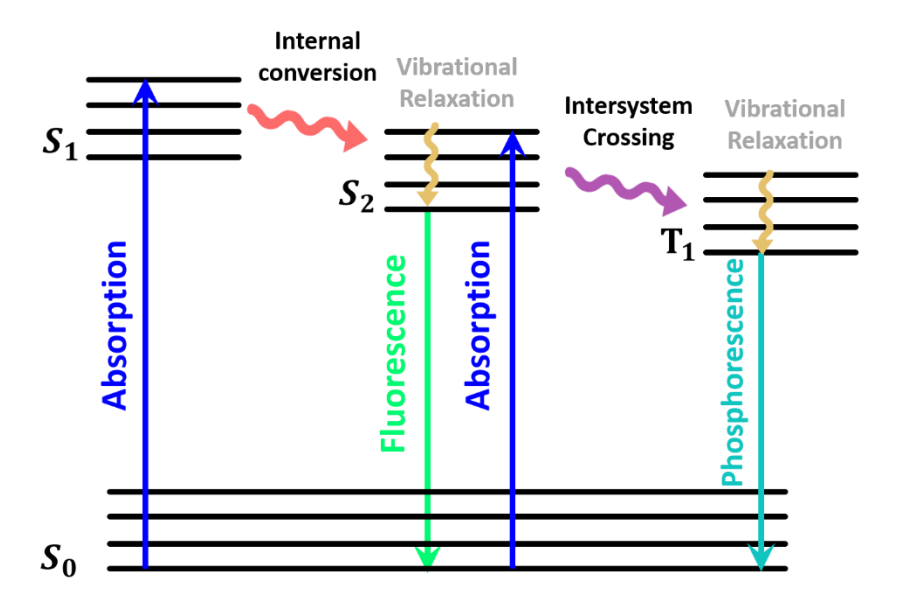


Figure 2. Typical Jablonski diagram to illustrate photoluminescent processes. The labels S0, S1 and S2 refer to the baseline singlet state, first singlet excited states and second singlet excited states, respectively, similarly T1 represents the first triplet excited state.

Förster resonance energy transfer (FRET)

FRET is an electrodynamic phenomenon that involves the non-radiative transfer of energy between two molecules: an excited donor molecule and an acceptor molecule. This energy transfer can only happen if the emission spectrum of the donor overlaps with the absorption spectrum of the acceptor. Specifically, the vibrational transitions in the donor molecule must align in energy with corresponding transitions in the acceptor molecule, as depicted in Figure 3. In the biosensing field, FRET is a useful phenomenon regarding its sensitivity for nano-scale distances between the molecules under study.⁶

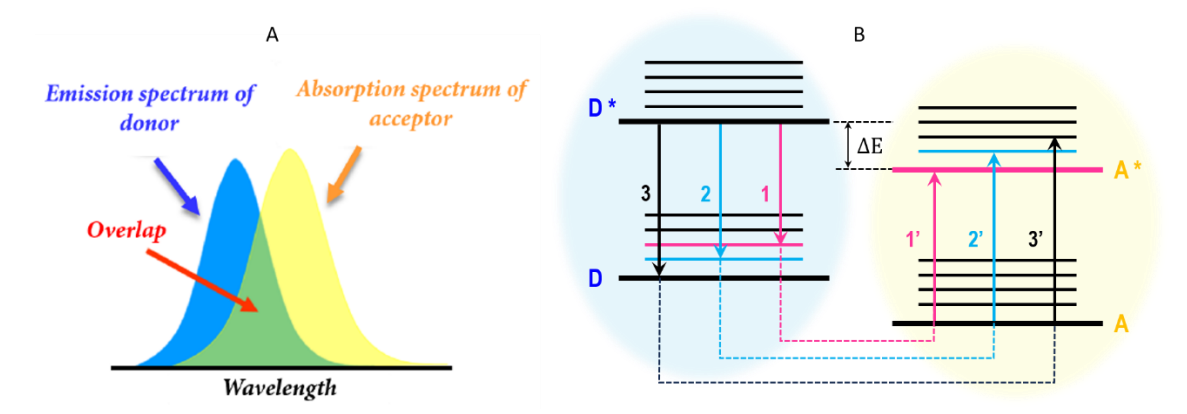


Figure 3. FRET A. Overlapping between the emission spectrum of the donor and the absorption of the acceptor. B. Energy level scheme of donor and acceptor molecules showing the coupled transitions. Donor molecule is illustrated in blue color and acceptor in yellow color. D* and A* refer to donor and acceptor in excited state respectively.

When FRET occurs, the electron in the excited donor molecule (D*), in our case Fluorescein isothiocyanate (FITC) returns to its ground state. Simultaneously, an electron in the acceptor molecule (A) in our case, graphene oxide (GO) moves to a higher excited-state orbital. If the acceptor molecule is fluorescent, it may emit light. However, if the acceptor is non-fluorescent, the energy is dissipated through other mechanisms, such as heat.

In general, the efficiency of FRET depends on the sixth power of the distance between the donor and acceptor molecules, as well as their relative orientation. Typically, the rate of transfer of excitation energy is described by the following expression:

$$k_T = \left(\frac{1}{\tau_d}\right) \left(\frac{R_0}{r}\right)^6 \tag{1}$$

Here, τ_d represents the fluorescence lifetime of the donor in the absence of the acceptor, r denotes the distance between the centers of the donor and acceptor molecules, and R_0 denotes the Förster distance, at which 50% of the excitation energy is transferred to the acceptor.

In FRET, the distance is typically large compared to the size of the molecule, allowing energy transfer to occur through space. This means that FRET does not require direct molecular contact between the donor and acceptor molecules. ⁵

It is important to mention that in the case of graphene, its nature as a 2-dimensional dipole modifies the expression (1) to an r^4 dependence.

The overlapping of spectra reflects the efficiency in energy transfer, e.g. if the overlap is bigger the donor increases the possibility to transfer energy to the acceptor. Overlap integral $I(\lambda)$, between the donor and the acceptor is given by:

$$J(\lambda) = \int_0^\infty F_D(\lambda) \,\epsilon_A(\lambda) \lambda^4 d\lambda \tag{2}$$

where $F_D(\lambda)$ is the normalized emission spectrum of the donor, $\epsilon_A(\lambda)$ corresponds to the molar absorption coefficient of the acceptor and λ is the wavelength.

Non-radiative energy transfer affects the fluorescence emission characteristics of the donor molecule. When the distance between the donor and acceptor is very small (a few Angstroms), the molecules come into contact, and their electron clouds can interact.

These orbital interactions are commonly known as electron exchange, as electrons can move between the molecules over short distances.⁸ Electron exchange is just one of several mechanisms that cause fluorescence quenching, which is defined as:

$$\mathbf{I} = \frac{I_f(t)}{I_0(t)} \tag{3}$$

and represents the attenuation of fluorescence intensity in a specific time frame. Here I_f corresponds to the final intensity of fluorescence and I_0 corresponds to the initial intensity of fluorescence.

1.3. GO and operating mechanism of FRET-GO based biosensor

Graphene is a carbon material characterized by its atomic thickness, classifying it as a two-dimensional material. It can be visualized as a flat sheet composed of carbon atoms arranged in a honeycomb lattice. This structure serves as the foundational framework for other carbon allotropes (see Figure 4).^{9,10}

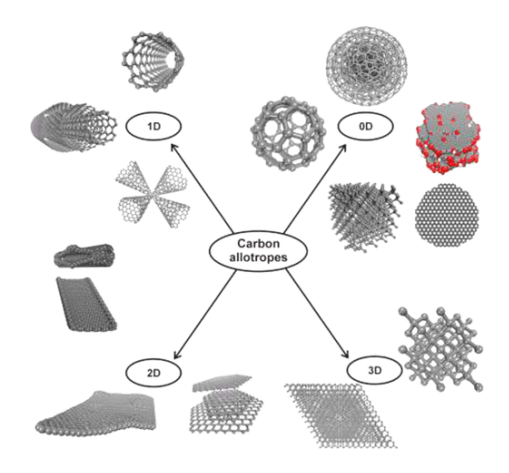


Figure 4. Allotropes of Carbon Adapted with permission from ⁹ Copyright © 2015 American Chemical Society

Additionally, the oxidized form of graphene, known as graphene oxide (GO), contains functional groups like hydroxyl, epoxy, carbonyl, and carboxyl groups. Specifically, GO features carboxyl groups at its edges and other oxygen-containing groups on the basal plane (see Figure 5). ¹¹ The Hummer method is the most commonly used technique to produce graphene oxide (GO). ¹²

Figure 5. Representation of the structure of GO Adapted with permission from ¹³. *Copyright* © *2019 American Chemical Society*

Notably, the surface chemistry of GO allows for the interaction of GO with proteins or DNA. ¹⁴ Furthermore, the literature highlights the remarkable optical properties of graphene oxide (GO). One notable feature is its broad spectral absorption range, making GO an ideal universal acceptor in Förster Resonance Energy Transfer (FRET) applications. ¹⁴ Our Real-Time biosensing platform consists in a surface coated with graphene oxide (GO) and a fluorescent bioprobe as a donor. The GO-coated surface has a strong affinity for bioprobes that do not interact with the analyte, resulting in quenched fluorescence when the analyte is absent. In contrast, fluorescent bioprobes that interact with the analyte do not experience quenching, as the bioprobe-analyte complex has no affinity for the GO-coated surface, and the analyte acts as a spacer between the GO-coated surface and the bioprobes (see Figure 6). This biosensing platform has also been previously employed to detect several analytes, including

human immunoglobulin G, prostate specific antigen, COVID-19 antibodies and *Escherichia coli*. ¹⁵

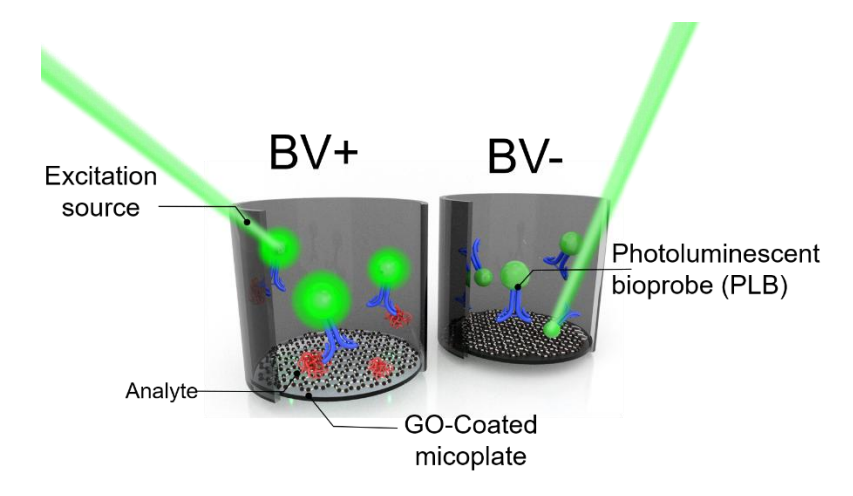


Figure 6. Operational mechanism of the biosensing platform.

1.4. Bacterial Vaginosis

Bacterial vaginosis (BV) occurs when the natural balance of bacteria in the vagina is disrupted. A balanced level of bacteria helps maintain vaginal health. However, when bacteria such as Gardnerella vaginalis overgrow, it can lead to bacterial vaginosis (see Figure 7). ¹⁶

BV can occur at any age but is most common during the reproductive years. Hormonal changes during this period can facilitate the overgrowth of specific types of bacteria. One of the enzymes that plays a significant role in the pathophysiology of BV is sialidase.

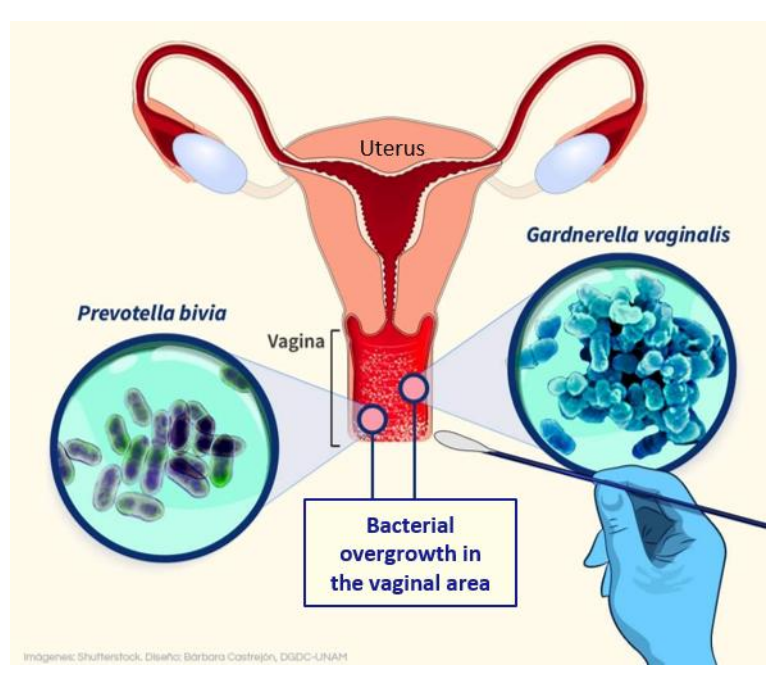


Figure 7. Bacterial Vaginosis illustration.

Adapted with permission from. ¹⁷ Shutterstock, Diseño: Bárbara Castrejón, DGDC-UNAM

Bacterial vaginosis is a common vaginal condition characterized by an imbalance in the vaginal flora, leading to the overgrowth of the aforementioned bacterial strains. Sialidase, an enzyme produced by these bacteria, plays a significant role in this illness. This enzyme cleaves sialic acids from glycoproteins, glycolipids, and polysaccharides on the surface of epithelial cells and mucins. Sialic acids are crucial for maintaining the integrity of the mucosal barrier in the vagina, and their removal by sialidase can disrupt this protective layer. ¹⁸ The activity of sialidase has been used as a biomarker to assess the severity of BV and its potential to cause adverse reproductive outcomes. ¹⁹

Detecting sialidase activity in vaginal secretions can be an important diagnostic tool for BV. It not only helps to confirm the diagnosis but also provides information on the severity of the condition and the risk of complications. Sialidase activity can be measured through biochemical assays that detect the enzyme's ability to cleave specific substrates.²⁰

1.5. Artificial intelligence (AI)

Artificial intelligence (AI) refers to the ability of machines and computer systems to perform tasks that typically require human intelligence. This includes learning, reasoning, problem-solving, visual and auditory perception, and natural language understanding, among other capabilities. AI involves the development of algorithms and computational models that can analyze data, learn patterns, and make decisions based on that data, such as Machine Learning and Deep Learning, see Figure 8. Currently, AI is applied across various fields, including medicine, economics, industrial automation, autonomous vehicles, virtual assistants, and more. ²¹

Machine learning

It is a crucial component of AI that enables systems to learn from their environment and apply that knowledge to make informed decisions. There are various algorithms that machine learning employs to iteratively learn, interpret, and enhance data for better predictive outcomes. These algorithms utilize statistical techniques to identify patterns and take actions based on these patterns. The most common machine learning algorithms include Supervised Learning, Unsupervised Learning, and Reinforcement Learning.²²

Deep Learning

Deep learning is a specific subfield of machine learning that emphasizes learning representations from data, focusing on successive layers of increasingly meaningful representations. The term "deep" in deep learning does not refer to a deeper understanding achieved by the approach but rather represents the idea of successive layers of representations. The depth of the model refers to the number of layers contributing to a data model. Other suitable names for this field could have been layered representation learning and hierarchical representation learning. Modern deep

learning often involves dozens or even hundreds of successive layers of representations, all learned automatically from exposure to training data.²²

In deep learning, these layered representations are usually learned (almost always) using models called neural networks, structured in literal layers stacked on top of each other. The term neural network refers to neurobiology, but while some core concepts of deep learning were partially inspired by our understanding of the brain, deep learning models are not models of the brain. ²²

A neural network (ANN) is made up of neurons arranged in layers, with connections (weights) and biases that modify the impact of inputs. Activation functions add non-linearity, allowing the network to recognize complex patterns. Its key components are illustrated in Figure 9.

Figure 8. Visual Breakdown of Key Areas in Artificial Intelligence.

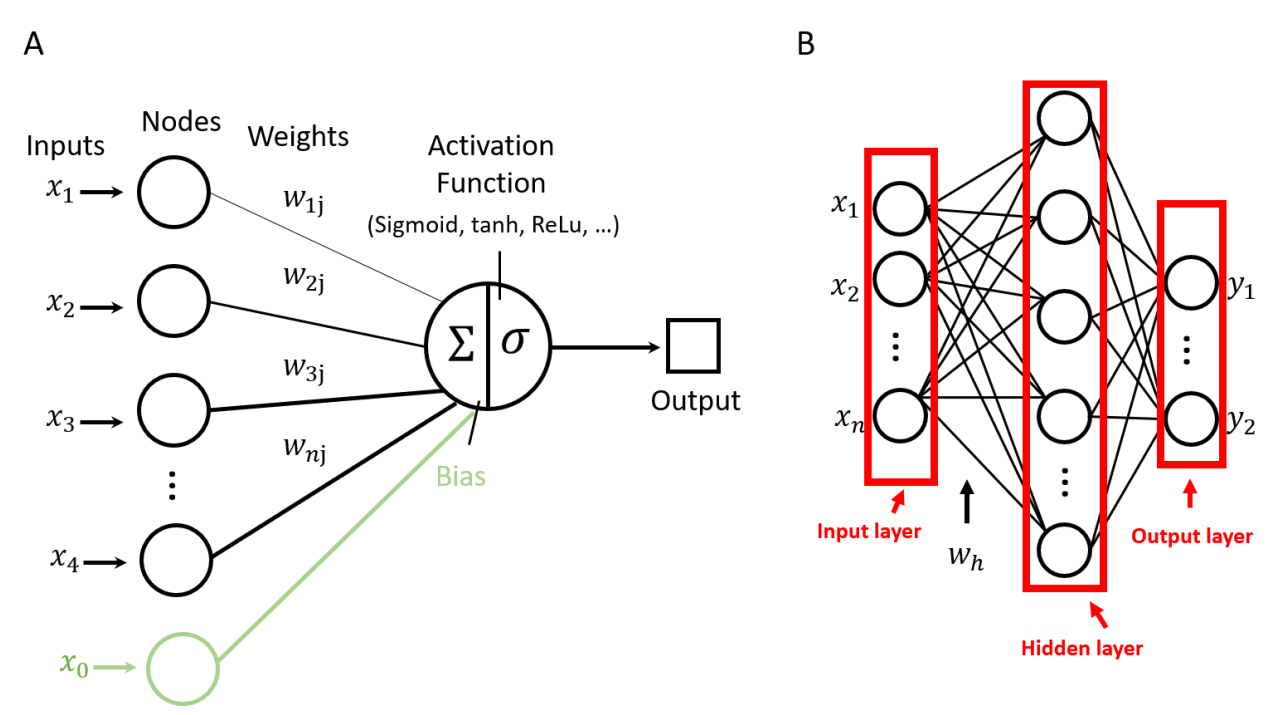


Figure 9. Main Parts of a Neural Network. A. Nodes. These are basic units that receive inputs, apply an activation function, and produce an output. Weights. Each connection between

neurons or nodes has a weight that adjusts the influence of one neuron on another. Bias. This is an additional parameter in a neuron that allows the activation function to be shifted (e.g. the left or right), which helps the model in fitting the data. Activation function. A mathematical function applied to the output of each neuron. It introduces non-linearity into the network, allowing it to learn complex patterns. B. Neurons are organized into layers, typically three types: Input layer: Receives external data and passes it to the network, Hidden layers: Process information gradually. Output layer: Generates the final output of the network after processing the information.

1.5.1. Basic functioning of an artificial neural network

The process is divided into two main stages: Forward Propagation and Back Propagation, both of which are crucial for training neural networks (see Figure 10).

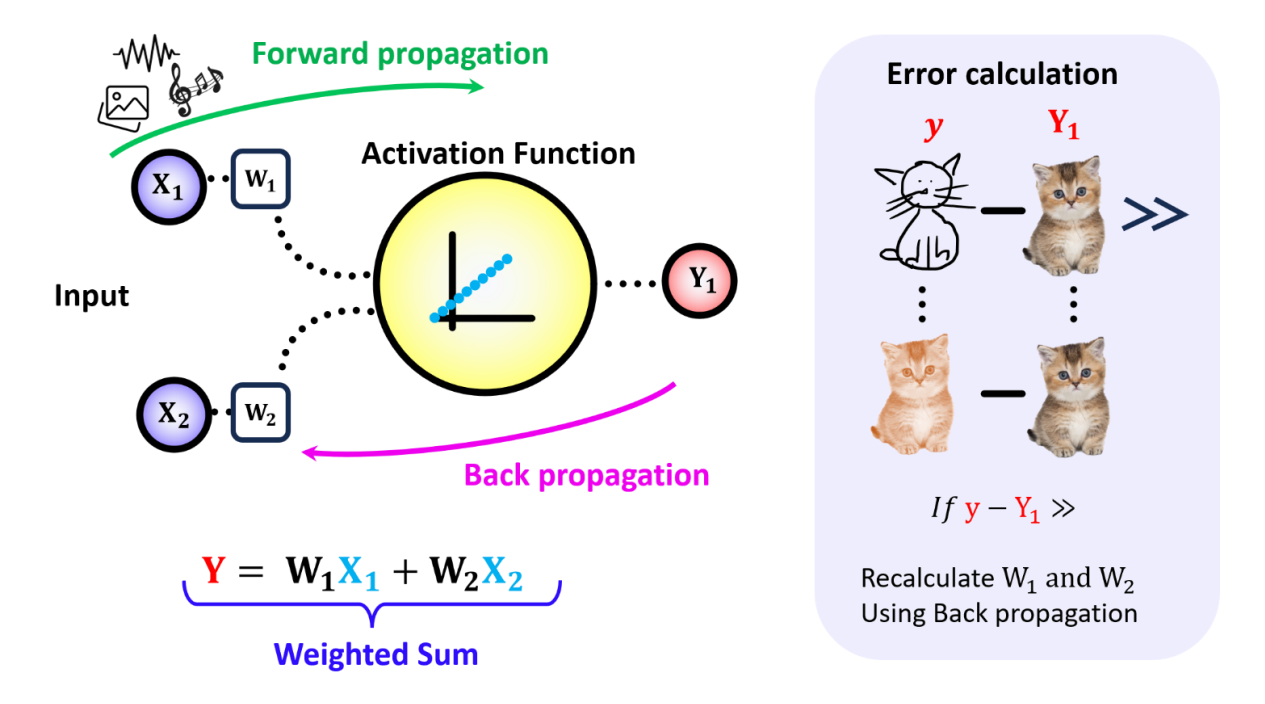


Figure 10. Schematic diagram of the basic functioning of an artificial neural network (perceptron).

In Forward Propagation, input data passes through the network layer by layer, from the input layer to the output layer. In each layer, the data is multiplied by the connection weights (weighted sum) and then passed through an activation function. The objective is to generate an output or prediction, which is subsequently compared to the actual target value to calculate the error. Back Propagation, on the other hand, focuses on adjusting the network's weights based on the error calculated during forward propagation. The error is propagated backward from the output layer to the previous layers, where gradients (derivatives) are calculated to determine how the weights should be updated to minimize the error. This adjustment is carried out using an optimization algorithm, such as gradient descent, to minimize the loss function and enhance the network's accuracy.

These stages work together to enable the neural network to learn patterns from data and make accurate predictions or classifications.²²

1.6. Artificial Neural Networks (ANNs) types

ANNs come in various forms, each designed for specific tasks and types of data. Below, some of the most common types of ANNs are illustrated in Figure 11 and described below.

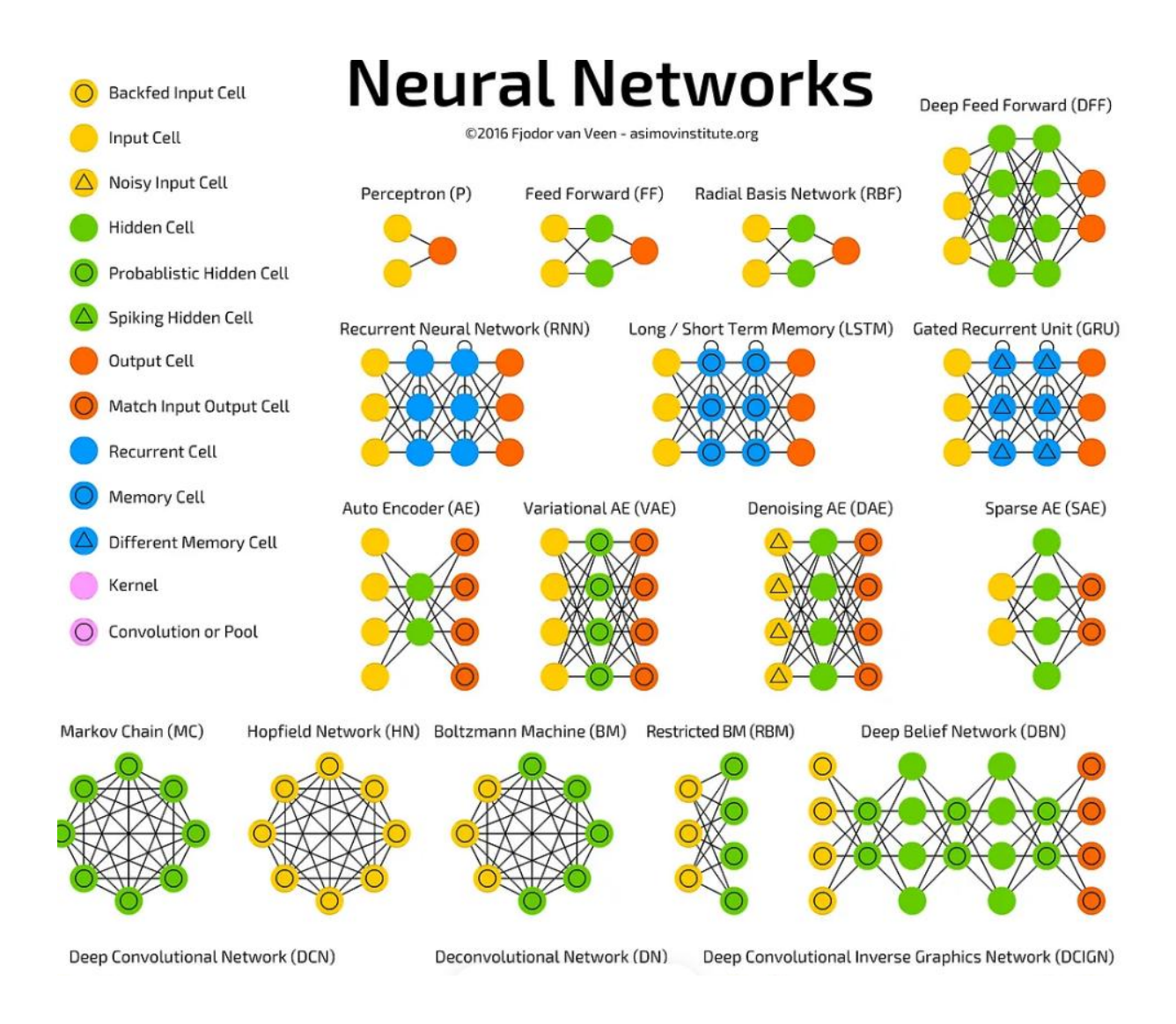


Figure 11. Neural Networks types. *Image adapted with permission of* ²³.

Feed forward Neural Network (FNN)

This is simplest type of ANN where the information flows in one direction, from input to output, without any cycles or loops. Usually is employed in basic pattern recognition, image classification, and simple regression tasks.

Convolutional Neural Network (CNN)

This is designed to process and analyze visual data. CNNs use convolutional layers to automatically and adaptively learn spatial hierarchies of features. Its main components are convolutional layers, pooling layers, and fully connected layers. Among the main applications are image and video recognition, image classification, object detection, and computer vision tasks.

Recurrent Neural Networks (RNNs)

RNNs are designed for sequential data processing. They feature connections that form directed cycles, enabling them to maintain a state and capture temporal dependencies. The key components include neurons with recurrent connections, which allow information to persist. RNNs are used in natural language processing, speech recognition, time series prediction, and other tasks involving sequential data.

Long Short-Term Memory (LSTM)

Networks are a specialized type of RNN that addresses the vanishing gradient problem. They use memory cells capable of maintaining their state over extended periods. Key components include memory cells, input gates, output gates, and forget gates. LSTMs are particularly effective for tasks requiring long-term dependencies, such as language modeling, machine translation, and speech recognition.

Multilayer Perceptrons (MLPs)

MLPs are a class of feedforward neural networks with multiple layers of neurons. MLPs can solve problems that are not linearly separable. They consist of an input layer, one or more hidden layers, and an output layer. MLPs are utilized for classification, regression, and complex pattern recognition.

Each type of ANN has its strengths and is suited for specific tasks, making them versatile tools in the field of machine learning and artificial intelligence. ²⁴. ²⁵

1.7. K-fold cross validation

It is a statistical method used to evaluate the performance of a machine learning model. In this technique, the dataset is divided into K equally sized subsets or "folds." The model is then trained and evaluated K times, each time using a different fold as the validation set and the remaining K-1 folds as the training set. This process ensures that every data point is used for both training and validation exactly once. By averaging the evaluation results from each fold, K-fold cross-validation provides a more accurate and reliable estimate of the model's performance, reducing the risk of overfitting and ensuring that the model generalizes well to unseen data. This method is particularly useful when dealing with limited datasets, as it maximizes the use of available data for both training and testing. A schematic diagram of this method is shown in the figure below.

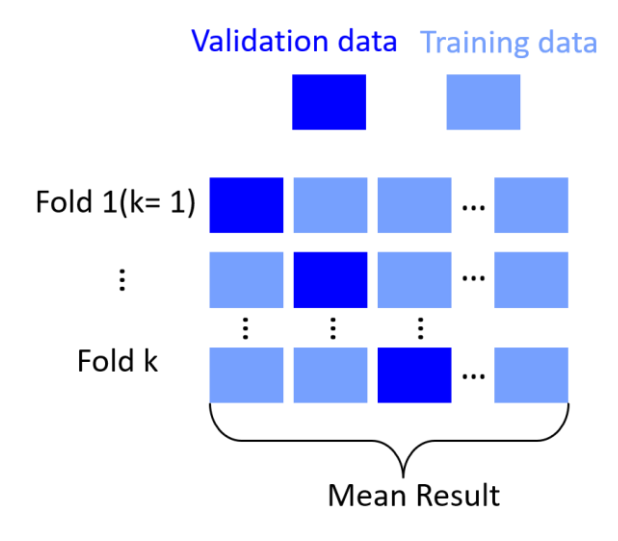


Figure 12. K-fold Cross Validation

1.8. Principal Component Analysis (PCA)

Principal Component Analysis (PCA) is a statistical technique used for dimensionality reduction in datasets with many features. It transforms the original variables into a new set of uncorrelated variables called principal components (see Figure 13), which are ordered by the amount of variance they capture from the data.

The first principal component captures the most variance, and each subsequent component captures progressively less. By focusing on the first few principal components, PCA simplifies the dataset, making it easier to analyze and visualize while retaining the most important information. ²⁷

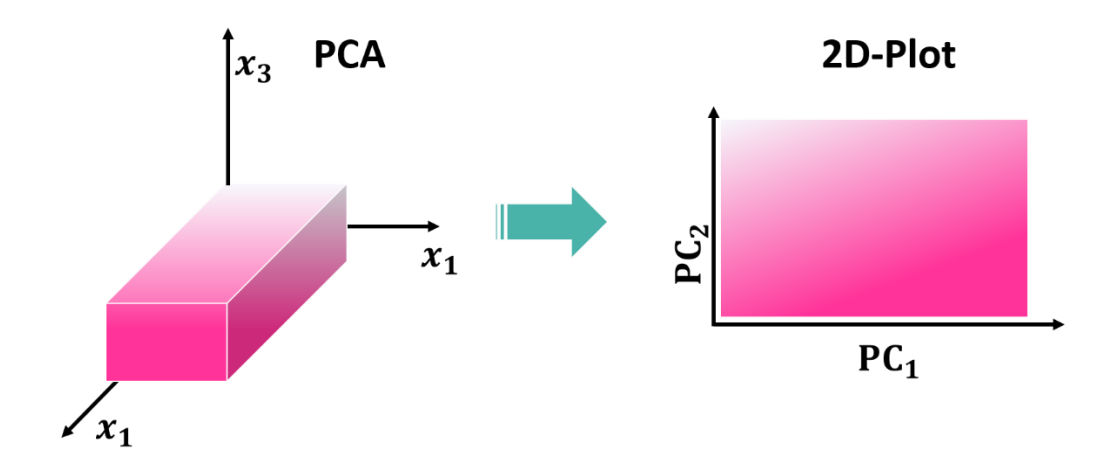


Figure 13. Dimensionality Reduction. Visualizing PCA's Transformation from 3D to 2D Space.

1.9. Evaluation metrics

These measures are used to determine or evaluate the performance of a classification model.

Confusion Matrix

Confusion matrices are commonly used in binary and multi-class classification problems. They allow us to visually and quantitatively evaluate the performance of a model. ²⁸

An example of a binary classification confusion matrix is depicted in the Figure below.

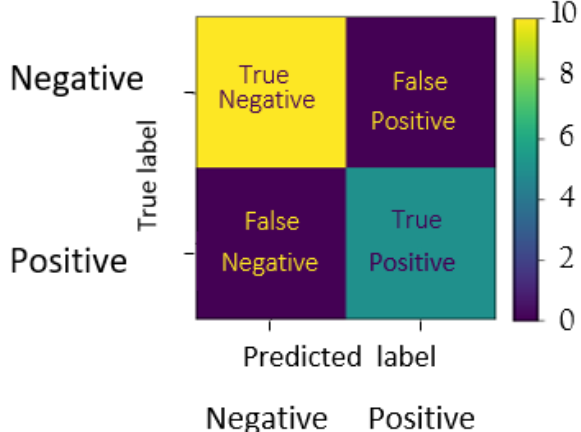


Figure 14. Confusion Matrix for binary classification. The term, True Positive (TP) refers to a sample belonging to the positive class being classified correctly, whereas, True Negative (TN) refers to a sample belonging to the negative class being classified correctly. Additionally, False Positive (FP) refers to a sample belonging to the negative class but being classified wrongly as a positive sample, and False Negative (FN) refers to a sample belonging to the positive class but being classified incorrectly as belonging to the negative class. It is important to note that the horizontal axis represents all prediction and the vertical axis represents all true values.

Using the number of false positives and false negatives, we can compute the sensitivity, specificity, precision, and accuracy of our model based on the mathematical expressions: ²⁹

% Recall (Sensitivity) =
$$\frac{TP}{TP + FN} \times 100$$
 [4]

% Specificity =
$$\frac{TN}{TN + FP} \times 100$$
 [5]

$$\%Precision = \frac{TP}{TP + FP} \times 100$$
 [6]

% Accuracy =
$$\frac{TP + TN}{Total Sample} \times 100$$
 [7]

The accuracy can be calculated by taking average of the values lying across the main diagonal.

In order determine the performance of the neural networks.

 F_1 score

Precision and sensitivity (also known as recall) are two crucial metrics, but they often conflict with each other. Precision measures the accuracy of positive predictions, while sensitivity evaluates the model's ability to capture all positive cases. The F1 score offers a balance between these two metrics, as it combines precision and sensitivity using the harmonic mean, as shown in the mathematical expression below:

$$F_{1} score = \frac{2 \times Precision \times Recall}{Precision + Recall}$$
 [8]

REFERENCES

- (1) Agarwal, T. *Biosensor Principle, Components, Types & Their Applications*. ElProCus Electronic Projects for Engineering Students. https://www.elprocus.com/what-is-a-biosensor-types-of-biosensors-and-applications/(accessed 2024-08-22).
- (2) Morales, M. A.; Halpern, J. M. Guide to Selecting a Biorecognition Element for Biosensors. *Bioconjugate Chem.* **2018**, *29* (10), 3231–3239. https://doi.org/10.1021/acs.bioconjchem.8b00592.
- (3) Selectivity in Analytical Chemistry. De Gruyter. https://www.degruyter.com/database/IUPAC/entry/iupac.73.0808/html (accessed 2024-08-22).
- (4) amersham pharmacia biotech. Fluor_ImagingPrinciples. https://www.bu.edu/picf/files/2010/10/Fluor-ImagingPrinciples.pdf.
- (5) Introduction to Fluorescence | David M. Jameson | Taylor & Francis eBo. https://www.taylorfrancis.com/books/mono/10.1201/b16502/introduction-fluorescence-david-jameson (accessed 2024-08-22).
- (6) Knox, R. S. Förster's Resonance Excitation Transfer Theory: Not Just a Formula. *J Biomed Opt* **2012**, *17* (1), 011003. https://doi.org/10.1117/1.JBO.17.1.011003.
- (7) Arnault, J.-C. Nanodiamonds: Advanced Material Analysis, Properties and Applications; 2017.
- (8) Principles of Fluorescence Spectroscopy | SpringerLink. https://link.springer.com/book/10.1007/978-0-387-46312-4 (accessed 2024-08-22).
- (9) Broad Family of Carbon Nanoallotropes: Classification, Chemistry, and Applications of Fullerenes, Carbon Dots, Nanotubes, Graphene, Nanodiamonds, and Combined Superstructures | Chemical Reviews. https://pubs.acs.org/doi/10.1021/cr500304f (accessed 2024-08-22).
- (10) Geim, A. K.; Novoselov, K. S. The Rise of Graphene. *Nature Mater* **2007**, *6* (3), 183–191. https://doi.org/10.1038/nmat1849.
- (11) Morales-Narváez, E.; Merkoçi, A. Graphene Oxide as an Optical Biosensing Platform. *Advanced Materials* **2012**, *24* (25), 3298–3308. https://doi.org/10.1002/adma.201200373.
- (12) Hummers, W. S. Jr.; Offeman, R. E. Preparation of Graphitic Oxide. *J. Am. Chem. Soc.* **1958**, *80* (6), 1339–1339. https://doi.org/10.1021/ja01539a017.
- (13) Sinclair, R. C.; Coveney, P. V. Modeling Nanostructure in Graphene Oxide: Inhomogeneity and the Percolation Threshold. *J. Chem. Inf. Model.* **2019**, *59* (6), 2741–2745. https://doi.org/10.1021/acs.jcim.9b00114.
- (14) Forster, Th. Energiewanderung und Fluoreszenz. *Naturwissenschaften* **1946**, *33* (6), 166–175. https://doi.org/10.1007/BF00585226.
- (15) Avila-Huerta, M. D.; Ortiz-Riaño, E. J.; Mancera-Zapata, D. L.; Cortés-Sarabia, K.; Morales-Narváez, E. Facile Determination of COVID-19 Seroconversion via Nonradiative Energy Transfer. *ACS Sens.* **2021**, *6* (6), 2136–2140. https://doi.org/10.1021/acssensors.1c00795.
- (16) Bautista, C. T.; Wurapa, E. K.; Sateren, W. B.; Morris, S. M.; Hollingsworth, B. P.; Sanchez, J. L. Association of Bacterial Vaginosis With Chlamydia and Gonorrhea

- Among Women in the U.S. Army. *Am J Prev Med* **2017**, *52* (5), 632–639. https://doi.org/10.1016/j.amepre.2016.09.016.
- (17) Innovador biosensor aplicado a la detección de la vaginosis bacteriana UNAM Global. https://unamglobal.unam.mx/global_revista/innovador-biosensor-aplicado-a-la-deteccion-de-la-vaginosis-bacteriana/ (accessed 2025-03-21).
- (18) Robinson, L. S.; Schwebke, J.; Lewis, W. G.; Lewis, A. L. Identification and Characterization of NanH2 and NanH3, Enzymes Responsible for Sialidase Activity in the Vaginal Bacterium Gardnerella Vaginalis. *J Biol Chem* **2019**, *294* (14), 5230–5245. https://doi.org/10.1074/jbc.RA118.006221.
- (19) Chen, L.; Li, J.; Xiao, B. The Role of Sialidases in the Pathogenesis of Bacterial Vaginosis and Their Use as a Promising Pharmacological Target in Bacterial Vaginosis. *Front Cell Infect Microbiol* **2024**, *14*, 1367233. https://doi.org/10.3389/fcimb.2024.1367233.
- (20) Rodríguez-Nava, C.; Cortés-Sarabia, K.; Avila-Huerta, M. D.; Ortiz-Riaño, E. J.; Estrada-Moreno, A. K.; Alarcón-Romero, L. del C.; Mata-Ruíz, O.; Medina-Flores, Y.; Vences-Velázquez, A.; Morales-Narváez, E. Nanophotonic Sialidase Immunoassay for Bacterial Vaginosis Diagnosis. *ACS Pharmacol. Transl. Sci.* **2021**, *4* (1), 365–371. https://doi.org/10.1021/acsptsci.0c00211.
- (21) Panch, T.; Szolovits, P.; Atun, R. Artificial Intelligence, Machine Learning and Health Systems. *J Glob Health* **2018**, 8 (2), 020303. https://doi.org/10.7189/jogh.08.020303.
- (22) *Deep Learning with Python*. Manning Publications. https://www.manning.com/books/deep-learning-with-python (accessed 2024-08-22).
- (23) The mostly complete chart of Neural Networks, explained | by Andrew Tch | Towards Data Science. https://towardsdatascience.com/the-mostly-complete-chart-of-neural-networks-explained-3fb6f2367464 (accessed 2024-08-25).
- (24) Ajit, A.; Acharya, K.; Samanta, A. A Review of Convolutional Neural Networks. In 2020 International Conference on Emerging Trends in Information Technology and Engineering (ic-ETITE); 2020; pp 1–5. https://doi.org/10.1109/ic-ETITE47903.2020.049.
- (25) Long Short-Term Memory Network an overview | ScienceDirect Topics. https://www.sciencedirect.com/topics/computer-science/long-short-term-memory-network (accessed 2023-07-14).
- (26) 3.1. Cross-validation: evaluating estimator performance. scikit-learn. https://scikit-learn/stable/modules/cross validation.html (accessed 2024-08-25).
- (27) Principal Component Analysis (PCA) Explained | Built In. https://builtin.com/data-science/step-step-explanation-principal-component-analysis (accessed 2023-06-28).
- (28) Ting, K. M. Confusion Matrix. In *Encyclopedia of Machine Learning*; Sammut, C., Webb, G. I., Eds.; Springer US: Boston, MA, 2010; pp 209–209. https://doi.org/10.1007/978-0-387-30164-8 157.
- (29) *sklearn.metrics.confusion_matrix*. scikit-learn. https://scikit-learn/stable/modules/generated/sklearn.metrics.confusion_matrix.html (accessed 2023-10-05).
- (30) F1 Score in Machine Learning: Intro & Calculation. https://www.v7labs.com/blog/f1-score-guide, https://www.v7labs.com/blog/f1-score-guide (accessed 2023-10-05).

Chapter 2.

Artificial intelligence in biosensing field: State of the art

Currently, numerous studies have demonstrated the immense potential of computing in enhancing the analytical performance of biosensing platforms. By identifying complex patterns within noisy signals, computing enables data inference from diverse sources such as medical, environmental, and traffic signals. Herein a brief overview of this field is provided.

On June 1, 2019, Aydogan Ozcan and his research team introduced their work utilizing Deep Learning to assist point-of-care biosensors. Later, in February 2020, they developed a biosensing analysis method based on particle aggregation to determine and quantify analytes, employing wide-field, lens-free computational microscopy powered by Deep Learning. ³¹ Additionally, bioinspired instruments that mimic olfactory and gustatory senses, such as artificial noses and tongues, have proven valuable in monitoring food spoilage, detecting environmental contaminants, and identifying viruses. These artificial systems effectively recognize and estimate analyte concentrations.³²

In late 2023, Ghumra et al. developed a biosensing system designed to directly detect SARS-CoV-2 in atmospheric aerosols. These systems are critical for mitigating pandemic impacts, emphasizing the importance of developing highly sensitive, specific, and efficient biosensing technologies.

In December 2023, Ammar Armghan published a study titled "Design of Biosensor for Synchronized Identification of Diabetes Using Deep Learning," ³³ where They explored the use of deep learning techniques to enhance the performance of glucose biosensors. By training neural networks on large datasets, the author demonstrated significant improvements in the accuracy and reliability of these sensors, a crucial

advancement for efficient diabetes management that enables more precise monitoring of glucose levels in patients.

In May 2024, Lanpeng Guo et al. published "Electrochemical Protein Biosensors for Disease Marker Detection: Progress and Opportunities,"³⁴ exploring the development of AI-enhanced electrochemical biosensors for real-time health biomarker monitoring. The integration of machine learning algorithms allows for the precise detection and quantification of biomarkers, with significant potential applications in personalized medicine. This approach supports the implementation of medical treatments tailored to the patient's unique biological responses, thereby optimizing the effectiveness of therapeutic interventions.

Finally, Ding et al., in their review titled "SERS-Based Biosensors Combined with Machine Learning for Medical Applications," ³⁵discussed recent advancements in the use of Surface-Enhanced Raman Spectroscopy (SERS) in combination with Machine Learning (ML). They highlight the application of these technologies in recognizing biological molecules, rapidly diagnosing diseases, developing innovative immunoassay techniques, and enhancing the semi-quantitative measurement capabilities of SERS. To sum up, several current biosensing systems are summarized in Table 1. ³⁶

Table 1. Machine learning for intelligent biosensing.

Biomarker	Biosensing mechanism	Platform	AI algorithm	Reference
Rabbit IgG	Paper-based colorimetric ELISA assays	Smartphone	GoogleNet	Duan et al (2023) 37
Lysozyme and	Fluorimetric	Nanosheets	SVM	Saberi et al. (2020) 38

Medical chemicals	Bacteriophage- based colorimetric sensing	Multi array sensor system	НСА	Kim et al (2020) ³⁹
ATP Blood glucose	Electronic-nose	Portable device	SVM	Boubin and Shrestha (2019) 40
Biomolecular	Tunnel junctions	Graphene nanoelectrodes	SVM	Puczkarski et al. (2017) ⁴¹
Albumin protein	LFA	Smartphone cameras	SVM	Foysal et al. (2019) 42
Physiological monitoring	Physical and biochemical sensing	Skin-friendly electronics	ANN	Zhang and Tao (2019)
Blood glucose (type 1 diabetics)	CGM	Wearable biosensors	SVM ARIMA, RF	Rodriguez- Rodriguez et. Al (2019) 43
Body fluid identification	SPR	SPRi device	PCA	Stravers et al. (2019) 44
NT-proBNP	Inmunoassay	Photonic crystal- enhance fluorescence	PCA, PLSR, SVM	Squire et al. (2019) ⁴⁵
Benzene, toluene formaldehyde	Electronic-nose	Sensor array chamber	SVM	Wang et al (2016) 46
VOCs	Fluorescent sensing	Cross- response sensor array	НСА	Lei et al (2015) ⁴⁷
Nasopharygneal cancer detection	SERS	Confoncal Raman micro- spectrometer	PCA, LDA	Feng et al. (2010) 48

Acronyms:

ELISA (Enzyme-Linked Immunosorbent Assay), **LFA** (Lateral Flow Assay, **CGM** (Continuous Glucose Monitoring), SPR (Surface plasmon resonance) and **SERS** (Surface Enhanced Raman Spectroscopy).

In conclusion, the integration of artificial intelligence into the field of biosensing has led to significant advancements in the accuracy, efficiency, and applicability of biosensors. The discussed approaches illustrate how AI is revolutionizing the biosensing field by enabling the development of smart biosensors and improving detection and monitoring capabilities across various biomedical and environmental applications. Ongoing interdisciplinary collaboration among data scientists, engineers, and biologists will remain crucial in driving these advancements and exploring new frontiers in biosensing.

REFERENCES

- 31) Greenbaum, A.; Zhang, Y.; Feizi, A.; Chung, P.-L.; Luo, W.; Kandukuri, S. R.; Ozcan, A. Wide-Field Computational Imaging of Pathology Slides Using Lens-Free on-Chip Microscopy. *Sci Transl Med* **2014**, *6* (267), 267ra175. https://doi.org/10.1126/scitranslmed.3009850.
- (32) Pal, S.; Kumar, D.; Ulucan-Karnak, F.; Narang, J.; Shukla, S. K. Bio-Inspired Electronic Sensors for Healthcare Applications. *Chemical Engineering Journal* **2024**, 499, 155894. https://doi.org/10.1016/j.cej.2024.155894.
- (33) Armghan, A.; Logeshwaran, J.; Sutharshan, S. M.; Aliqab, K.; Alsharari, M.; Patel, S. K. Design of Biosensor for Synchronized Identification of Diabetes Using Deep Learning. *Results in Engineering* **2023**, *20*, 101382. https://doi.org/10.1016/j.rineng.2023.101382.
- (34) Guo, L.; Zhao, Y.; Huang, Q.; Huang, J.; Tao, Y.; Chen, J.; Li, H.-Y.; Liu, H. Electrochemical Protein Biosensors for Disease Marker Detection: Progress and Opportunities. *Microsyst Nanoeng* **2024**, *10*, 65. https://doi.org/10.1038/s41378-024-00700-w.
- (35) Ding, Y.; Sun, Y.; Liu, C.; Jiang, Q.-Y.; Chen, F.; Cao, Y. SERS-Based Biosensors Combined with Machine Learning for Medical Application. *ChemistryOpen* **2023**, *12* (1), e202200192. https://doi.org/10.1002/open.202200192.
- (36) Ghumra, D. P.; Shetty, N.; McBrearty, K. R.; Puthussery, J. V.; Sumlin, B. J.; Gardiner, W. D.; Doherty, B. M.; Magrecki, J. P.; Brody, D. L.; Esparza, T. J.; O'Halloran, J. A.; Presti, R. M.; Bricker, T. L.; Boon, A. C. M.; Yuede, C. M.; Cirrito, J. R.; Chakrabarty, R. K. Rapid Direct Detection of SARS-CoV-2 Aerosols in Exhaled Breath at the Point of Care. *ACS Sens* **2023**, *8* (8), 3023–3031. https://doi.org/10.1021/acssensors.3c00512.
- (37) Duan, S.; Cai, T.; Zhu, J.; Yang, X.; Lim, E. G.; Huang, K.; Hoettges, K.; Zhang, Q.; Fu, H.; Guo, Q.; Liu, X.; Yang, Z.; Song, P. Deep Learning-Assisted Ultra-Accurate

- Smartphone Testing of Paper-Based Colorimetric ELISA Assays. *Analytica Chimica Acta* **2023**, *1248*, 340868. https://doi.org/10.1016/j.aca.2023.340868.
- (38) Saberi, Z.; Rezaei, B.; Rezaei, P.; Ensafi, A. A. Design a Fluorometric Aptasensor Based on CoOOH Nanosheets and Carbon Dots for Simultaneous Detection of Lysozyme and Adenosine Triphosphate. *Spectrochimica Acta Part A: Molecular and Biomolecular Spectroscopy* **2020**, *233*, 118197. https://doi.org/10.1016/j.saa.2020.118197.
- (39) Kim, C.; Lee, H.; Devaraj, V.; Kim, W.-G.; Lee, Y.; Kim, Y.; Jeong, N.-N.; Choi, E. J.; Baek, S. H.; Han, D.-W.; Sun, H.; Oh, J.-W. Hierarchical Cluster Analysis of Medical Chemicals Detected by a Bacteriophage-Based Colorimetric Sensor Array. *Nanomaterials* **2020**, *10* (1), 121. https://doi.org/10.3390/nano10010121.
- (40) Ahmed, A.; Aziz, S.; Abd-alrazaq, A.; Farooq, F.; Househ, M.; Sheikh, J. The Effectiveness of Wearable Devices Using Artificial Intelligence for Blood Glucose Level Forecasting or Prediction: Systematic Review. *Journal of Medical Internet Research* **2023**, *25* (1), e40259. https://doi.org/10.2196/40259.
- (41) *Graphene nanoelectrodes for biomolecular sensing* | *Journal of Materials Research*. https://link.springer.com/article/10.1557/jmr.2017.256 (accessed 2024-08-25).
- (42) Foysal, K. H.; Seo, S. E.; Kim, M. J.; Kwon, O. S.; Chong, J. W. Analyte Quantity Detection from Lateral Flow Assay Using a Smartphone. *Sensors* **2019**, *19* (21), 4812. https://doi.org/10.3390/s19214812.
- (43) Rodríguez-Rodríguez, I.; Rodríguez, J.-V.; Chatzigiannakis, I.; Zamora Izquierdo, M. Á. On the Possibility of Predicting Glycaemia 'On the Fly' with Constrained IoT Devices in Type 1 Diabetes Mellitus Patients. *Sensors* **2019**, *19* (20), 4538. https://doi.org/10.3390/s19204538.
- (44) Stravers, C. S.; Gool, E. L.; van Leeuwen, T. G.; Aalders, M. C. G.; van Dam, A. Multiplex Body Fluid Identification Using Surface Plasmon Resonance Imaging with Principal Component Analysis. *Sensors and Actuators B: Chemical* **2019**, *283*, 355–362. https://doi.org/10.1016/j.snb.2018.12.050.
- (45) Squire, K. J.; Zhao, Y.; Tan, A.; Sivashanmugan, K.; Kraai, J. A.; Rorrer, G. L.; Wang, A. X. Photonic Crystal-Enhanced Fluorescence Imaging Immunoassay for Cardiovascular Disease Biomarker Screening with Machine Learning Analysis. *Sensors and Actuators B: Chemical* **2019**, 290, 118–124. https://doi.org/10.1016/j.snb.2019.03.102.
- (46) Wang, H.; Hu, Z.; Long, F.; Guo, C.; Yuan, Y.; Yue, T. Early Detection of *Zygosaccharomyces Rouxii*—Spawned Spoilage in Apple Juice by Electronic Nose Combined with Chemometrics. *International Journal of Food Microbiology* **2016**, 217, 68–78. https://doi.org/10.1016/j.ijfoodmicro.2015.10.010.
- (47) Sun, X.; Wang, Y.; Lei, Y. Fluorescence Based Explosive Detection: From Mechanisms to Sensory Materials. *Chem. Soc. Rev.* **2015**, *44* (22), 8019–8061. https://doi.org/10.1039/C5CS00496A.
- (48) Feng, S.; Chen, R.; Lin, J.; Pan, J.; Chen, G.; Li, Y.; Cheng, M.; Huang, Z.; Chen, J.; Zeng, H. Nasopharyngeal Cancer Detection Based on Blood Plasma Surface-Enhanced Raman Spectroscopy and Multivariate Analysis. *Biosensors and Bioelectronics* **2010**, *25* (11), 2414–2419. https://doi.org/10.1016/j.bios.2010.03.033.

Chapter 3.

Experimental set up

3.1. Neural Network Implementation for Sialidase detection.

Artificial neural networks (ANNs) have become a powerful tool for classifying and diagnosing medical conditions using complex data. To optimize the analytical performance of our biosensing platform, a neural network model was implemented to classify vaginal samples as either BV-negative or BV-positive. The implementation details are presented in this chapter.

3.1.1. Reagents and equipment

Jupiter Notebook as an integrated development environment (IDE), along with the following libraries:

- Numpy
- Tensorflow
- Matplotlib
- Sklearn

3.1.2. Dataset collection

A total of 162 clinical samples were classified as BV positive (BV+) or BV negative (BV-) based on the Amsel criteria, a standard diagnostic method for BV. Of these, 54 samples were BV+ and 108 were BV-. The clinical samples were then combined with photoluminescent probes in a GO-coated microwell for kinetic analysis of fluorescence quenching levels. This process is depicted in Figure 15.²⁰

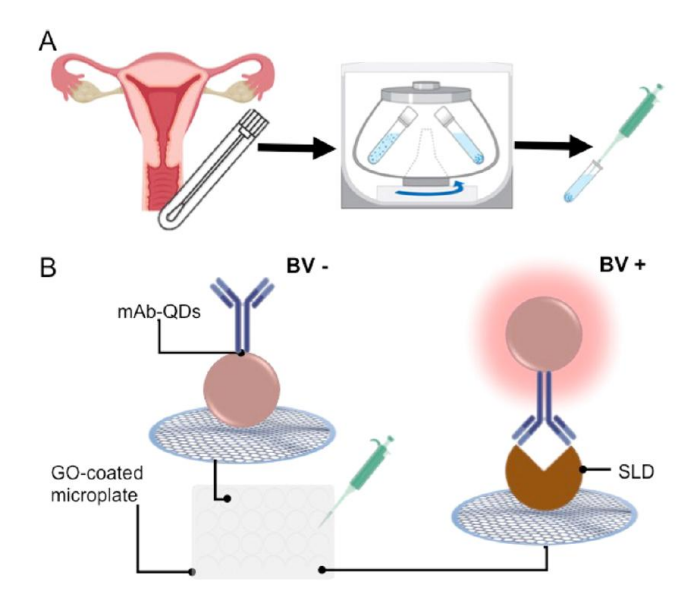


Figure 15. Sample Preparation and Biosensing Platform for SLD Detection Using nanoBVA sample is collected from the vaginal sac fundus using a sterile swab and placed in a sodium chloride saline solution for storage. The sample is then centrifuged to remove cellular debris, and the supernatant is aspirated for analysis. B. Biosensing Platform Targeting SLD (nanoBV). The clinical sample is diluted (1:4) and mixed with a nanoconjugate (mAbQDs) in a GO-coated microwell. Typically, negative samples (BV−) show quenched nanoconjugates due to nonradiative energy transfer caused by the affinity between mAb-QDs and the GO-coated microwell. In contrast, positive samples (BV+) exhibit strong fluorescence, which can be quantified, as the SLD/mAb-QDs complex lacks affinity for the GO-coated microwell. Taken with permission from ²⁰ Copyright © 2021 American Chemical Society

3.2. DATASET ARRANGEMENT

The dataset was generated based on fluorescence quenching ratios measured using the nanophotonic immunoassay: I_f/I_0 . Here, I_0 denotes the fluorescence intensity of the sample at time 0, and I_f represents the intensity at time f. Data were collected at 5-minute intervals over 120 minutes, ⁴⁹ resulting in a matrix with 162 rows and 20 columns, 162 representing the number of samples and 20 corresponding to the measurements (features) of the I_f/I_0 values. This data series is available on the GitHub repository, as shown in Figure 16 A.

This series of data is publicly available on GitHub repository. ⁵⁰

To analyze the temporal patterns in the collected data and identify optimal time intervals for binary classification (BV+ or BV-), we divided the dataset into four groups: G₁, G₂, G₃, and G₄. Each group consists of five measurements representing 25-minute intervals. Thus, G₁ covers the first 25 minutes, G₂ covers 25 to 50 minutes, and so on, covering the entire 120-minute experimental period. A schematic illustration of this partitioning is provided in Figure 16 B.

We also explored the possibility of using 20 and 30-minute time intervals for the groups (See Tables 11 -12 in Appendix); however, the groups with 25-minute intervals proved to be more suitable.

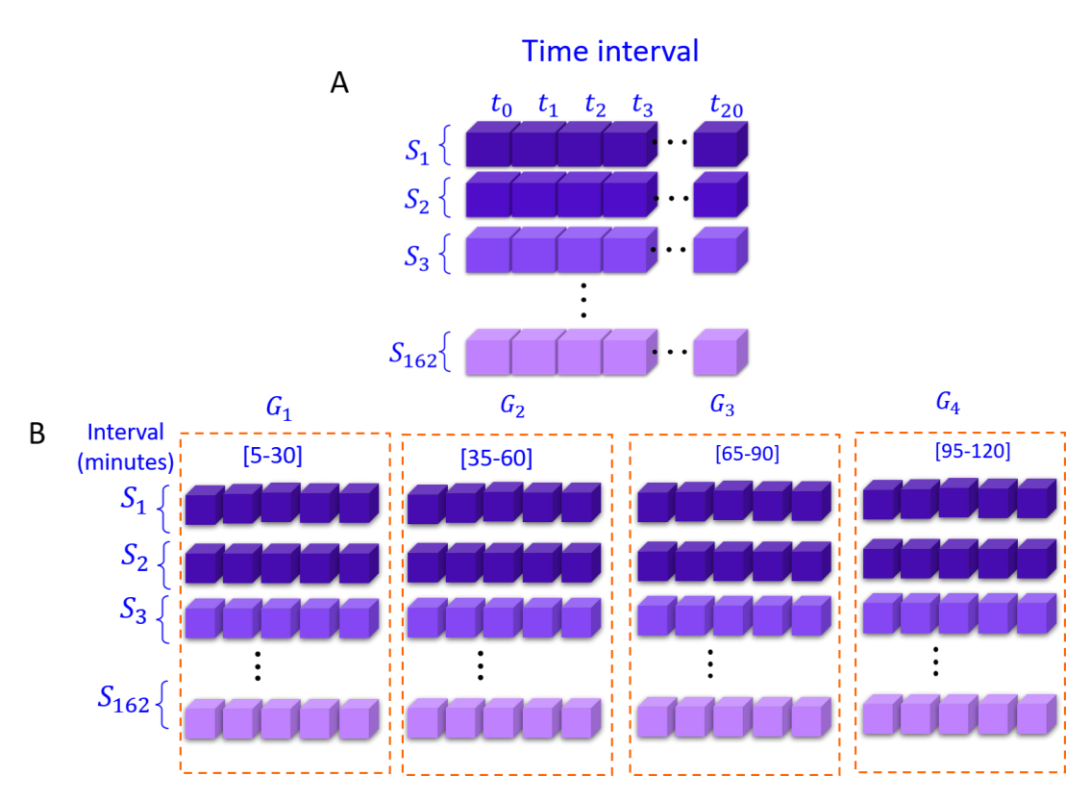


Figure 16. A. Dataset matrix B. Dataset splitting.

3.2.1. Normalization

Prior to the training of the neural architectures, the data set was normalized according to Equation 1, as this contributes to the convergence of the networks and thus to the significant improvement of the results.

$$x = \frac{x - \mu}{\sigma} \quad [9]$$

here x is the input data, μ is the mean and σ the standard deviation of the fluorescence quenching levels of a given sample.

3.3. 2-D VISUALIZATION OF THE DATA

Prior to training the neural network architectures, we used principal component analysis (PCA) to reduce the dimensionality of the data and create a 2D distribution plot. This approach enabled us to observe correlations in the data based on their analytical behavior.

A script for PCA as well as fluorescence level data was shared on GitHub repository.

3.4. TRAINING PROCESS

The performance of the neural network architectures was assessed using the K-fold cross-validation technique. This method ensures a robust and generalized evaluation by employing various combinations of training and validation data at each step. The dataset was divided into percentages of 70%, 15%, and 15% for training, validation, and testing, respectively. Figure 12 in Chapter 2 provides a visual representation of this technique. Given the volume of our data, K-fold cross-validation was most effective with k = 10, meaning the data were divided into 10 folds. With 54 positive and 108 negative samples, each fold contained 10 negative and 5 positive samples. This partitioning was essential for accurately interpreting the confusion matrices later in Chapter 4.

3.4.1. ANNs implementation

Neural network architectures, including MLPs, LSTMs, and CNNs, were trained as supervised learning tasks, ⁵¹ with each sample labeled as either BV+ or BV- according to the Amsel criteria. ²⁰ In the developed script, positive samples (BV+) were represented by a vector of ones (54 x 1) and negative samples (BV-) by a vector of zeros (108 x 1). These vectors were combined to form a new vector of dimensions 162 x 1.

Model performance was optimized by adjusting various hyperparameters such as the number of layers, neurons, activation functions, and regularization rates (see Table 2).

3.5. Feature selection.

After identifying the optimal architecture for the BV classification task, we utilized 1D-CNN to emphasize the most relevant features of the data and identify the optimal time interval. We used the data groups from the PCA analysis G_1 , G_2 , G_3 , and G_4 . To maximize dataset, use and understand group behavior, we implemented the 1D-CNN model and systematically combined the four individual datasets. For example, $G_{1,2}$ represents the combination of groups G_1 and G_2 , while $G_{2,3}$ denotes the merger of G_2 and G_3 , and so on.

3.6. Determination of clinical sensitivity and specificity.

The sensitivity, specificity, precision, and accuracy of our model were calculated based on the counts of false positives, false negatives, true positives, and true negatives from the classification results. We used the Python library *sklearn.metrics* in our script, ⁵⁰ which applies the formulas outlined in Equations [4-7]. Additionally, we computed the F1 score, an evaluation metric that combines precision and sensitivity (or recall), as specified in Equation [8].

REFERENCES

- (49) Ortiz-Riaño, E. J.; Mancera-Zapata, D. L.; Ulloa-Ramírez, M.; Arce-Vega, F.; Morales-Narváez, E. Measurement of Protein Kinetics Using a Liquid Phase-Based Biosensing Platform. *Anal. Chem.* **2022**, *94* (45), 15553–15557. https://doi.org/10.1021/acs.analchem.2c03305.
- (50) Diana Lorena Mancera; Fernando Arce Vega; Eden Morales Narváez. Git Hub Repository. https://github.com/BioNanosensors/AI_Biosensor/blob/main/SD_classifiers_Matrix.ip ynb.
- (51) Cunningham, P.; Cord, M.; Delany, S. J. Supervised Learning. In *Machine Learning Techniques for Multimedia: Case Studies on Organization and Retrieval*; Cord, M., Cunningham, P., Eds.; Cognitive Technologies; Springer: Berlin, Heidelberg, 2008; pp 21–49. https://doi.org/10.1007/978-3-540-75171-7_2.
- (52) Nearest Centroid Classifier. https://cran.r-project.org/web/packages/lolR/vignettes/nearestCentroid.html (accessed 2024-08-29).
- (53) Kingma, D. P.; Ba, J. Adam: A Method for Stochastic Optimization. arXiv January 29, 2017. https://doi.org/10.48550/arXiv.1412.6980.
- (54) M, H.; M.N, S. A Review on Evaluation Metrics for Data Classification Evaluations. *IJDKP* **2015**, *5* (2), 01–11. https://doi.org/10.5121/ijdkp.2015.5201.
- (55) Wibawa, A. P.; Utama, A. B. P.; Elmunsyah, H.; Pujianto, U.; Dwiyanto, F. A.; Hernandez, L. Time-Series Analysis with Smoothed Convolutional Neural Network. *Journal of Big Data* **2022**, *9* (1), 44. https://doi.org/10.1186/s40537-022-00599-y.
- (56) Ismail Fawaz, H.; Forestier, G.; Weber, J.; Idoumghar, L.; Muller, P.-A. Deep Learning for Time Series Classification: A Review. *Data Min Knowl Disc* **2019**, *33* (4), 917–963. https://doi.org/10.1007/s10618-019-00619-1.
- (57) Livieris, I. E.; Pintelas, E.; Pintelas, P. A CNN–LSTM Model for Gold Price Time-Series Forecasting. *Neural Comput & Applic* **2020**, *32* (23), 17351–17360. https://doi.org/10.1007/s00521-020-04867-x.
- (58) Jin, X.; Yu, X.; Wang, X.; Bai, Y.; Su, T.; Kong, J. Prediction for Time Series with CNN and LSTM. In *Proceedings of the 11th International Conference on Modelling, Identification and Control (ICMIC2019)*; Wang, R., Chen, Z., Zhang, W., Zhu, Q., Eds.; Lecture Notes in Electrical Engineering; Springer: Singapore, 2020; pp 631–641. https://doi.org/10.1007/978-981-15-0474-7 59.

Chapter 4.

Results and discussion

As previously discussed, using the Amsel criteria as a reference for BV determination, BV was diagnosed with clinical specificity and sensitivity of c.a. 96 %, respectively, by means of a conventional analysis of the data offered by our real-time immunoassay.²⁰ Following the methods detailed in the Experimental Section, we demonstrate that the series of data delivered by a real-time immunoassay can be useful to feed artificial neural networks and enhance the specificity and sensitivity.

Firstly, PCA allowed for the visualization of the 2D distribution of our data set as a function of the principal components over the execution of the nanophotonic immunoassay. Figure 17 illustrates how the samples correlate with each other throughout time. In particular, we observed that the G₄ group composed by the last time interval (95 - 120 minutes) displays a clear division between the BV+ and BV- samples. The use of the nearest centroid classifier ⁵² allowed us to quantitatively confirm that, over time, the dataset shows a marked difference between the BV+ and BV- classes. This was evidenced by the fact that the separation between the centroids of each class increased over time, reaching a maximum separation at 120 minutes.

This observation was a starting point to determine an optimal interval objectively.

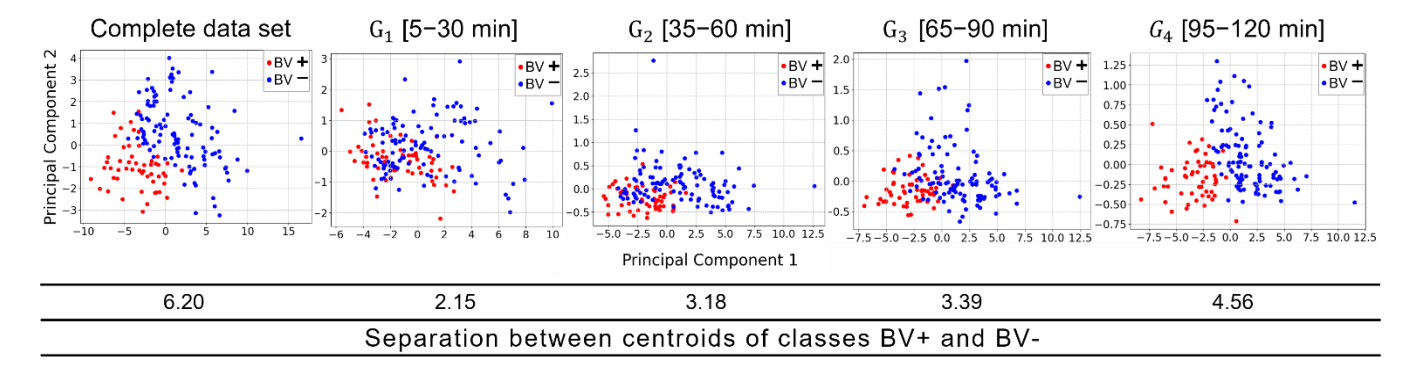
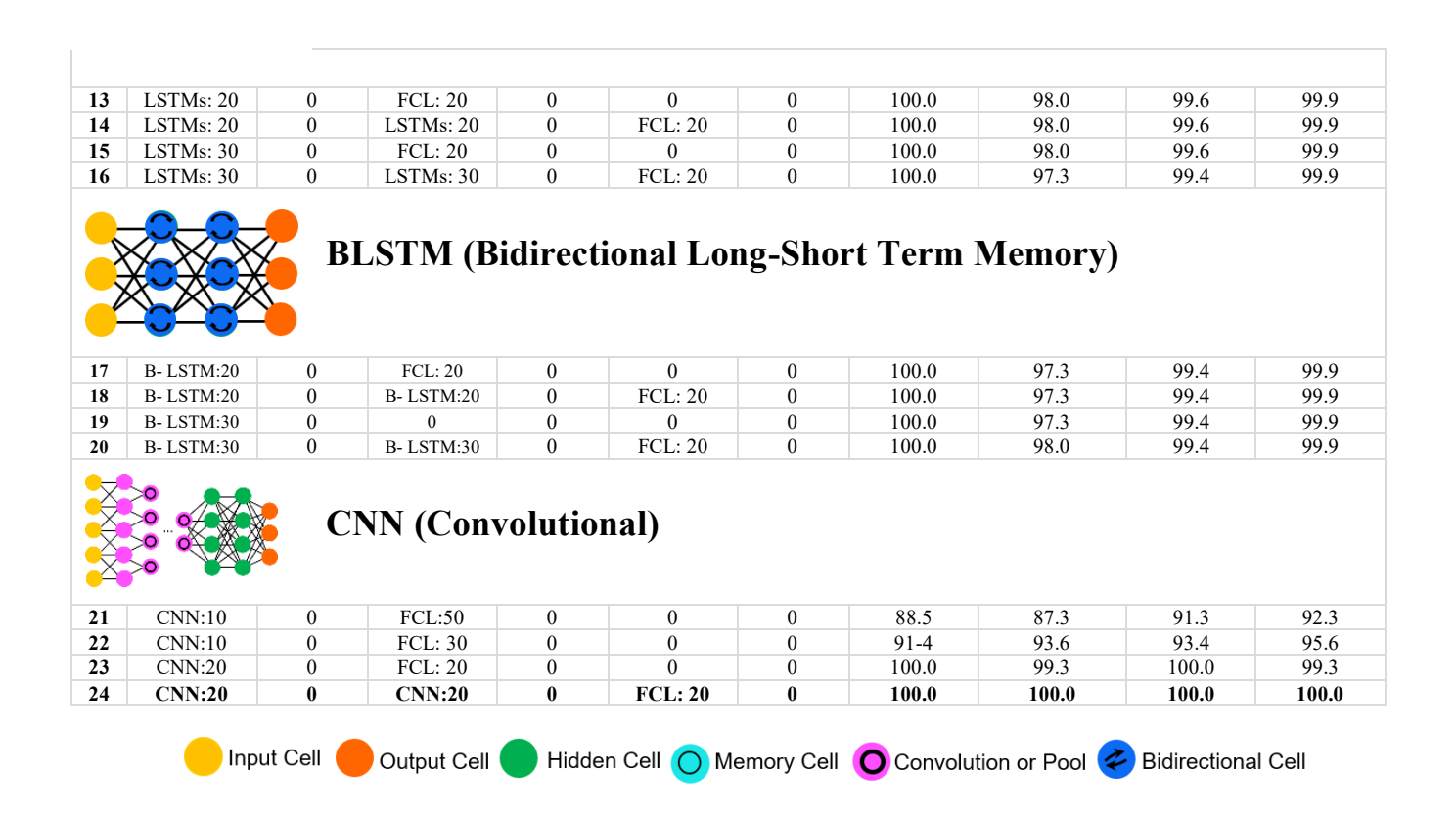


Figure 17. PCA and distances between the classes BV+ and BV- (for the complete data and for different times data sets).

Table 2 presents the performance results of the 24 neural networks assessed in this study, as detailed in the Experimental Section. The 1D-CNN model, which features two 1D-CNN layers with 20 neurons each in the first and second hidden layers, and a third layer with 20 fully connected neurons, emerged as the most effective for BV diagnosis. This model achieved a perfect accuracy rate of 100% in both validation and training stages. Initial training results, with 70% of the data allocated for training, 15% for validation, and 15% for testing, also showed optimal performance (see Figure 19 and Table 6).

Table 2. Performances of the tested architectures assessed with 10-fold cross-validation.

eurons		neurons		Number of neurons	-	(%)	(%)	(%)	(%)
	MI	L P (Mul t	tilayer	Perceptr	on)				
CL: 10	0	FCL: 50	0	0	0	92.5	87.5	92.6	83.3
CL: 20	0	0	0	0	0	98.4	96.6	98.1	98.3
CL: 20	0	FCL: 20	0	0	0	100.0	96.6	99.4	99.8
CL: 20	0.1	FCL: 20	0.1	0	0	100.0	97.3	99.4	99.8
CL: 20	0.2	FCL: 20	0.2	0	0	100.0	96.6	99.2	99.8
CL: 20	0.3	FCL: 20	0.3	0	0	100.0	96.6	99.1	99.8
CL: 30	0	FCL: 0	0	0	0	99.3	96.6	99.0	99.2
CL: 30	0	FCL: 30	0	0	0	100.0	96.6	99.2	99.8
CL: 30	0.1	FCL: 30	0.1	0	0	100.0	97.3	99.4	99.9
CL: 30	0.2	FCL: 30	0.2	0	0	100.0	98.0	99.6	99.9
CL: 30	0.3	FCL: 30	0.3	0	0	99.3	98.0	99.2	99.9
CL: 50	0	FCL: 50	0	0	0	95.5	93.4	96.3	96.3
	CL: 20 CL: 20 CL: 20 CL: 20 CL: 20 CL: 20 CL: 30 CL: 30 CL: 30 CL: 30 CL: 30	CL: 10 0 CL: 20 0 CL: 20 0 CL: 20 0 CL: 20 0.1 CL: 20 0.2 CL: 20 0.3 CL: 30 0 CL: 30 0 CL: 30 0 CL: 30 0.1 CL: 30 0.2 CL: 30 0.3	CL: 10 0 FCL: 50 CL: 20 0 0 CL: 20 0 FCL: 20 CL: 20 0.1 FCL: 20 CL: 20 0.2 FCL: 20 CL: 20 0.3 FCL: 20 CL: 30 0 FCL: 30 CL: 30 0 FCL: 30 CL: 30 0 FCL: 30 CL: 30 0.1 FCL: 30 CL: 30 0.1 FCL: 30 CL: 30 0.1 FCL: 30 CL: 30 0.2 FCL: 30 CL: 30 0.3 FCL: 30	CL: 10	CL: 10	CL: 20	CL: 10	CL: 10	CL: 10



Note: Architectures were trained using Adam optimizer ⁵³ with a batch size of 16 and 200 epochs. It was set and initial learning rate of 0.001.

Moreover, as shown in Table 3, LSTM and 1D-CNN architectures demonstrated the highest accuracy in diagnosing BV. The mean F_1 score 54 for the LSTM architecture was 0.97, while the CNN architecture achieved a mean F_1 score of 1.0. Additionally, the B-LSTM architecture obtained an F_1 score of 0.96, and the MLP architecture scored 0.92. These findings align with previous research comparing CNNs, MLPs, and LSTMs for time series forecasting, which indicated that CNNs and LSTMs generally performed better in classification tasks than MLPs. $^{55-58}$

Table 3. F₁ score for each fold in the MLP, LSTM, B-LSTM and 1D-CNN architectures

Fold MLP LSTM B-LSTM 1D-CNN

			F ₁ score	
1	1.00	1.00	1.00	1.00
2	1.00	1.00	1.00	1.00
3	0.91	1.00	0.91	1.00
4	0.89	0.89	0.89	1.00
5	0.83	0.91	0.91	1.00
6	0.91	1.00	1.00	1.00
7	0.91	0.89	1.00	1.00
8	0.80	1.00	1.00	1.00
9	1.00	1.00	0.91	1.00
10	0.91	1.00	1.0	1.00
Mean	0.92	0.97	0.96	1.00

As discussed above, PCA demonstrated that group G₄ generated less overlapping area between BV+ and BV- samples. This is reflected in a clear boundary between BV+ and BV- groups. This finding is consistent with the validation and training percentages (see content highlighted in bold in Table 4), as well as with the conclusions drawn in the conventional method for BV diagnosis based on a concentration threshold, where the biosensing platform showed superior performance, that is, only considering those data collected at the end of the immunoassay (120 minutes).

Table 4. Performance of the best architecture, the 1D-CNN, for the time groups G_1 , G_2 , G_3 and G_4 . The most relevant data are marked in bold.

Gro	up	Accuracy in training (%)	Accuracy in validation (%)	Sensitivity in all data (%)	Specificity in all data (%)
	G_1	81.7	70.0	76.0	82.5

G_2	84.7	77.3	76.8	87.9
G_3	90.8	88.0	83.5	94.5
G_4	98.7	97.3	99.6	98.0
$G_{1,2,3,4}$	100	100	100	100

We also explored the performance of our AI-assisted approach by using combinations between groups, which showed that group $G_{4,1}$ offered the highest percentages in training and validation accuracy, when compared with the other group combinations, see Table 5. Actually, the performance with $G_{4,1}$ was better than that obtained using the G_4 group; particularly, in terms of training and validation accuracy, G_4 obtained values of 98.7% and 97.3% respectively, while $G_{4,1}$ obtained 99.8% and 99.3%, respectively, suggesting that the combination of initial and final measurements provided the most relevant information in this AI-assisted approach. A visual representation of this experiment can be found in Figure 18.

Table 5. Performance of the 1D-CNN architecture fed with different combinations of data groups. The most relevant data are marked in bold.

	Accuracy	Accuracy		
Graun	in	in	Sensitivity	Specificity
Group	training	validation	(%)	(%)
	(%)	(%)		
$G_{1,2}$	89.96	74.66	72.0	78.9
$G_{1,3}$	93.87	87.33	86.0	88.0
$G_{2,3}$	93.19	86.66	88.0	90.0
$G_{2,4}$	98.97	96.66	96.0	98.0
$G_{3,4}$	99.0	97.30	98.0	96.0
$G_{4,1}$	99.8	99.3	98.00	97.0

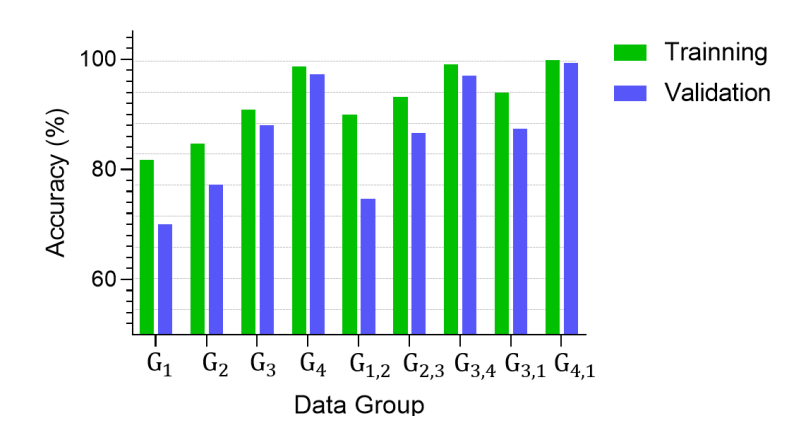


Figure 18. Bar chart depicting the performance of the 1D-CNN architecture fed with different combinations of data groups.

Confusion matrices in Figure 19-23, aside from being an evaluation metric, provided a graphical representation of the model's performance in a classification task, i.e., Figure 19 shows that the 1D-CNN architecture achieves 100% accuracy in the classification task since it did not obtain false positives or false negatives in any of the 10 folds.

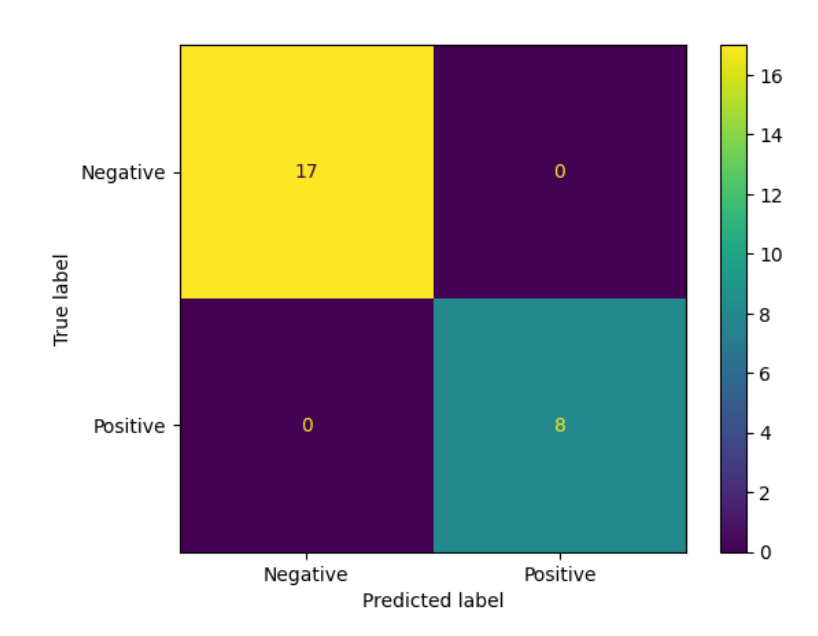


Figure 19. The resultant confusion matrix of the training, 70% of the data was used for the training set, 15% for the validation set, and 15% for the testing set.

Table 6. Results of the training process

	Accuracy					
Training	Validation	Testing	Sensitivity	Specificity	F ₁ score	
1.00	1.00	1.00	1.00	1.00	1.00	

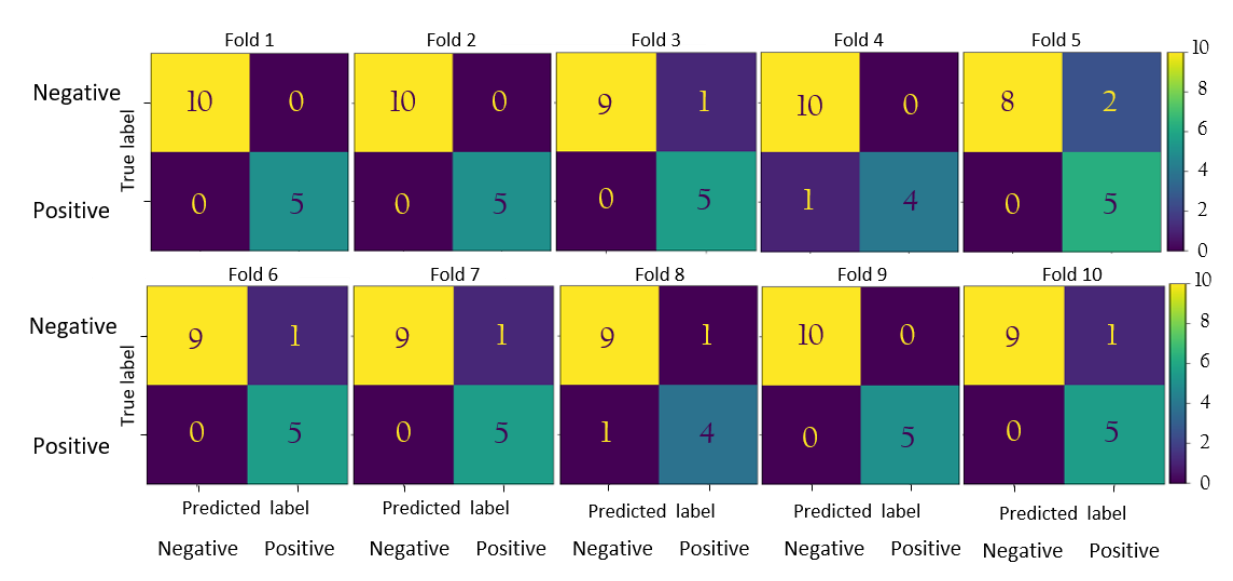


Figure 20. Confusion matrices for each fold in MLP architecture. MLP architecture made a classification without errors in folds 1 and 2, whereas in folds 3, 6, 7 and 10, it classified a negative sample as positive, in fold 4 it classified a positive sample as negative, in fold 5 it presented two false positives and finally, in fold 8 it presented a false positive and a false negative.

Table 7. F₁ Score for each fold in MLP architecture.

Fold	1	2	3	4	5	6	7	8	9	10	Mean
F1 Score	1.00	1.00	0.91	0.89	0.83	0.91	0.91	0.80	1.00	0.91	0.92

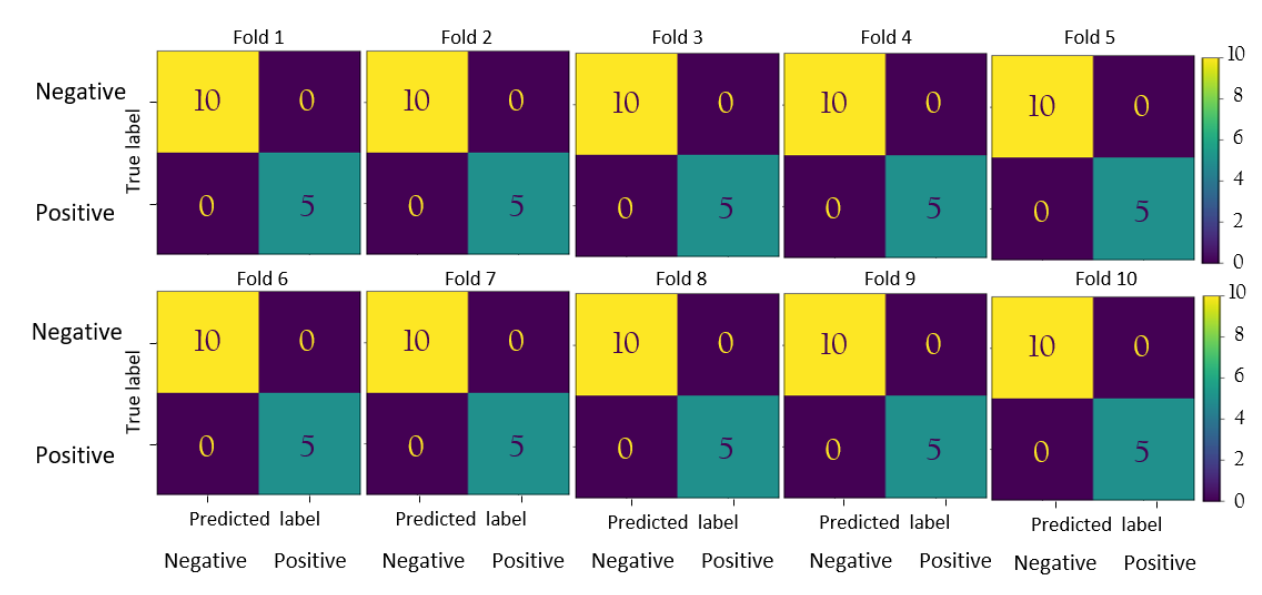


Figure 21. Confusion matrices for each fold in CNN architecture. 1D-CNN architecture achieves 100% accuracy in the classification task since it did not obtain false positives or false negatives in any of the 10 folds.

Table 8. F₁ Score for each fold in CNN architecture.

Fold	1	2	3	4	5	6	7	8	9	10	Mean
F1 Score	1.00	1.00	1.00	1.00	1.00	1.00	1.00	1.00	1.00	1.00	1.00

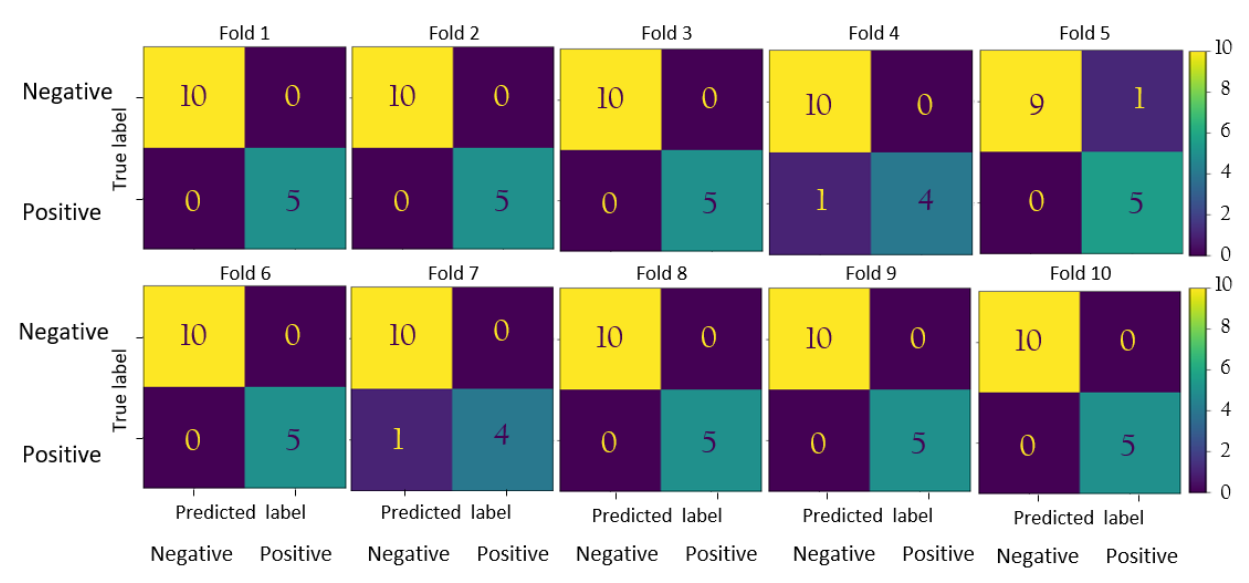


Figure 22. Confusion matrices for each fold in LSTM architecture. LSTM architecture in folds 1, 2, 3, 6, 8, 9 and 10 correctly classifies both the 10 negative samples and the 5

positive samples. On the other hand, in fold 4 ,out of 5 positive samples, it classifies 1 as negative and in fold 5 out of 10 negative it classifies 1 as positive.

Table 9. F₁ Score for each fold in LSTM architecture.

Fold	1	2	3	4	5	6	7	8	9	10	Mean
F1 Score	1.00	1.00	1.00	0.89	0.91	1.00	0.89	1.00	1.00	1.00	0.97

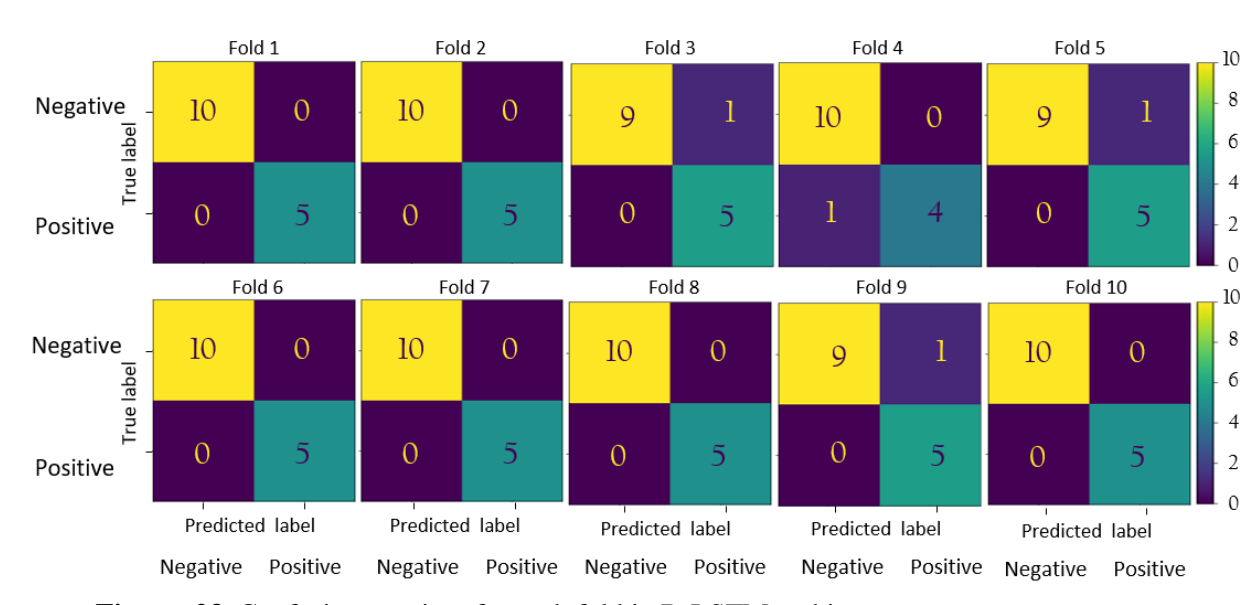


Figure 23. Confusion matrices for each fold in B-LSTM architecture.

Table 10. F₁ Score for each fold in B- LSTM architecture.

Fold	1	2	3	4	5	6	7	8	9	10	Mean
F1 Score	1.00	1.00	0.91	0.89	0.91	1.00	1.00	1.00	0.91	1.00	0.96

Chapter 5

Conclusions

In this study, we confirmed that the clinical sensitivity and specificity of a real-time biosensing system can be enhanced by implementing neural networks, with CNN and LSTM architectures outperforming MLPs in classifying time-varying datasets due to their ability to capture and retain time-series features. This AI-assisted approach not only removed the need to establish biomarker concentration thresholds for diagnosis through a real-time immunoassay but also significantly boosted clinical sensitivity and specificity, achieving up to 100% in binary classification.

Additionally, we demonstrated that machine learning techniques are valuable for identifying optimal testing times in a real-time biosensing platform. Although the increase in sensitivity and specificity from 96% to 100% might seem modest, it is particularly significant when applied to large populations, where it could lead to accurate diagnoses for hundreds or even thousands of patients. Overall, by harnessing real-time data on the binding interactions between biorecognition elements and analytes, this AI-assisted approach can be adapted for diagnosing other medical conditions using real-time immunoassays targeting specific biomarkers.

Chapter 6

Appendix

6.1. Performance of the 1D-CNN architecture fed with groups of 20 and 30 min intervals.

Table 11. Performance of the 1D-CNN architecture fed with groups of 20 min intervals.

Group	Accuracy in training (%)	Accuracy in validation (%)	Sensitivity in all data (%)	Specificity in all data (%)
G_1	79.8	68.3	60.0	50.0
G_2	83.4	74.6	81.0	80.0
G_3	90.6	88.0	80.0	92.0
G_4	89.0	84.6	86.9	80.0
G_5	98.7	97.3	98.0	96.0

Table 12. Performance of the 1D-CNN architecture fed with groups of 30 min intervals.

Group	Accuracy in training (%)	Accuracy in validation (%)	Sensitivity in all data (%)	Specificity in all data (%)
G_1	83.8	71.3	80.0	20.0
G_2	91.4	89.3	84.0	92.0
G_3	92.9	87.3	100	80
G_4	98.0	97.0	99.0	94.0

6.2. Image Segmentation Process Using U-NET Architecture

U-NET is a neural network model designed for computer vision tasks, specifically for segmentation problems.

Dr. Mariana Ávila developed a microfluidic analytical device (μ PAD) that determines if a liquid sample contains a specific analyte by measuring the quenching rate (see Figure 3a). To achieve this, Mariana measures intensity density in specific regions of the device as shown in Figure 3b and calculates the quenching rate according to the mathematical expression [10]. The goal of this part of the project is to implement a neural network that can identify the areas of interest for calculating the fluorescence quenching rate simply by inputting a set of images into the network.

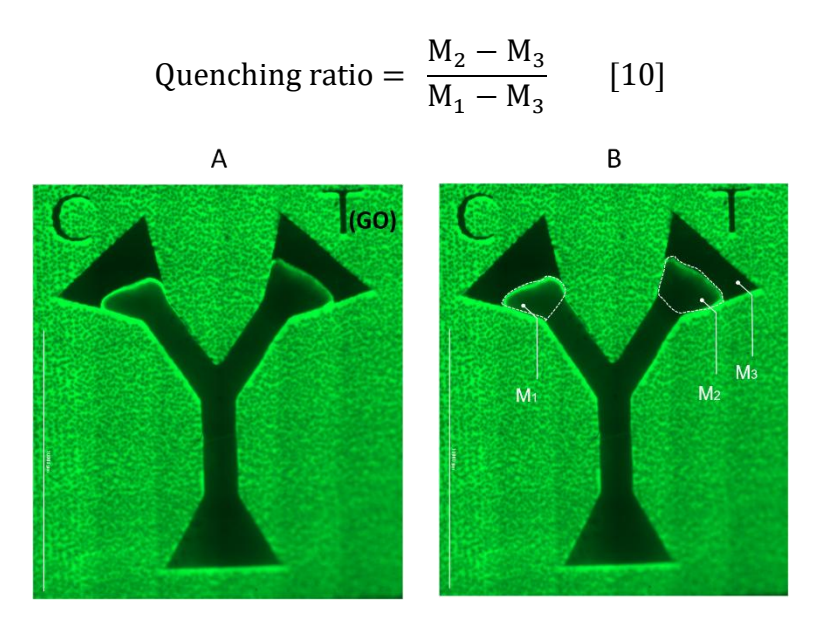


Figure 24. Paper-Based Microfluidic Analytical Device. A. The operation of this system. It involves a liquid sample flowing through the main channel to reach the Control (C) and Test (T) zones. The fluid does not completely cover the device; the upper ends of the Control and Test zones are mostly left dry. B. Measurements. M_1 , M^2 , and M_3 correspond to intensity density measurements of the wet areas in the Control and Test zones, respectively, while M_3 refers to the dry area.

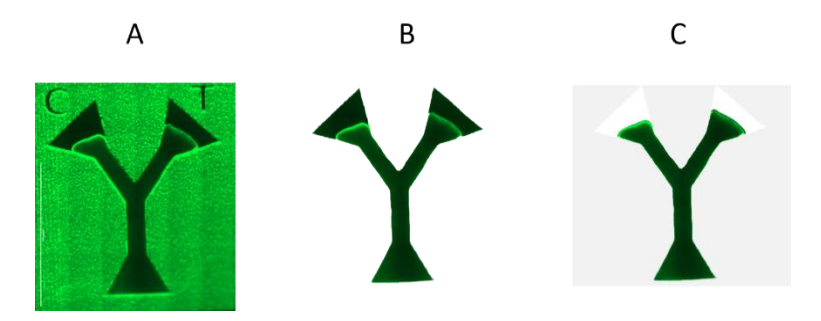


Figure 25. Segmentation Process. The first step for the network to determine the presence of an analyte is to recognize the shape of the microfluidic device. To achieve this, the network is trained with images like the one on the left (A). Subsequently, to differentiate between the dry areas (painted white) and the areas with the liquid sample, training images like the one on the right (B) are used.

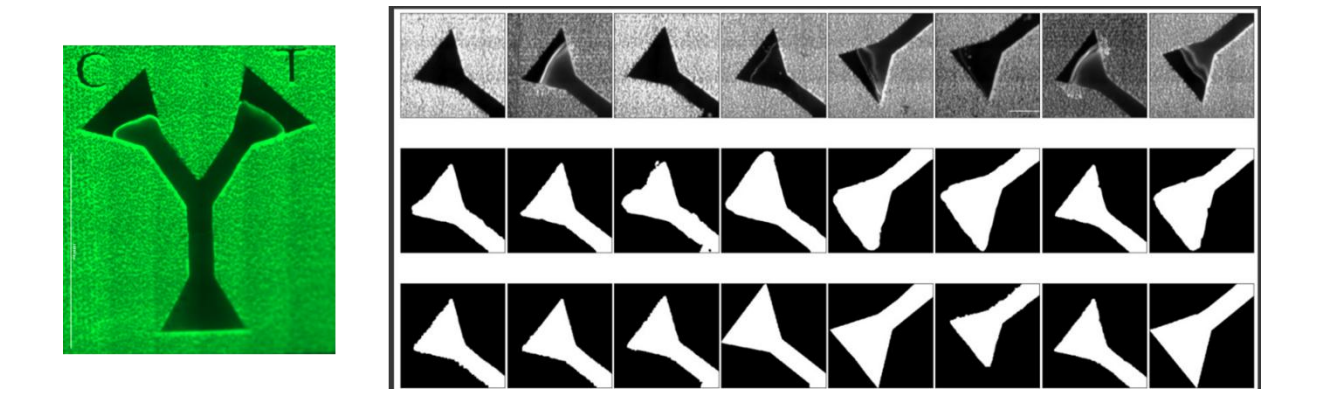


Figure 26. First predictions of the μ PAD shape

6.3. Kinetic Binding Constants

Kinetic binding constants, known as the association constant (Ka) and the dissociation constant (Kd), are fundamental parameters in the process of bio-recognition.

Association Constant (Ka)

The binding process occurs when a protein and its respective ligand collide with the correct orientation. The association constant describes the rate at which the direct reaction occurs to form the protein-ligand complex. This rate depends on the

concentration of the protein and the ligand and is measured in units of inverse molar concentration per second.

Dissociation Constant (Kd)

This constant describes the rate at which the protein-ligand complexes dissociate. This rate is independent of the concentrations of free proteins and ligands in the system and is measured in s⁻¹.

Measuring the kinetic binding constants such as Ka and Kd is crucial in biosensing, as the affinity of antibodies for the target analyte is essential for ensuring high sensitivity during detection.

The developed network uses preprocessed measurements to fit a function that allows associating the parameters with the association and dissociation constants. In this case, the function used is known as "One Phase Association" (see Figure)

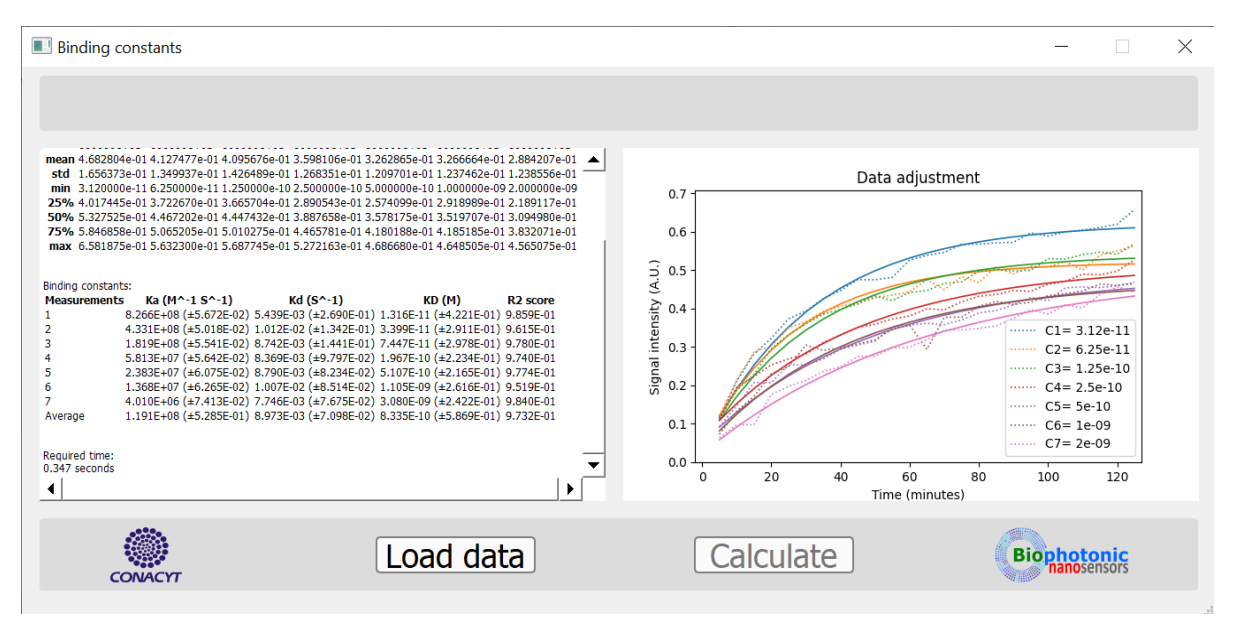


Figure 27. Graphical interface developed for determining association and dissociation constants in H-IgG samples, with association and dissociation constants displayed on the left side.